

2007

## The design and fabrication of high performance optical interference filters for the mid-infrared region

Emily Marie Fehrman Cory  
*University of Dayton*

Follow this and additional works at: [https://ecommons.udayton.edu/graduate\\_theses](https://ecommons.udayton.edu/graduate_theses)

---

### Recommended Citation

Fehrman Cory, Emily Marie, "The design and fabrication of high performance optical interference filters for the mid-infrared region" (2007). *Graduate Theses and Dissertations*. 2612.  
[https://ecommons.udayton.edu/graduate\\_theses/2612](https://ecommons.udayton.edu/graduate_theses/2612)

This Thesis is brought to you for free and open access by the Theses and Dissertations at eCommons. It has been accepted for inclusion in Graduate Theses and Dissertations by an authorized administrator of eCommons. For more information, please contact [mschlangen1@udayton.edu](mailto:mschlangen1@udayton.edu), [ecommons@udayton.edu](mailto:ecommons@udayton.edu).

THE DESIGN AND FABRICATION OF HIGH PERFORMANCE OPTICAL  
INTERFERENCE FILTERS FOR THE MID-INFRARED REGION

Thesis

Submitted to

The School of Engineering of the

UNIVERSITY OF DAYTON

In Partial Fulfillment of the Requirements for

The Degree

Master of Science in Electro-Optics

By

Emily Marie Fehrman

UNIVERSITY OF DAYTON

Dayton, Ohio

May, 2007

THE DESIGN AND FABRICATION OF HIGH PERFORMANCE OPTICAL  
INTERFERENCE FILTERS FOR THE MID-INFRARED REGION

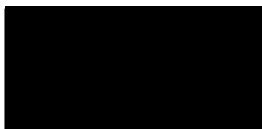
APPROVED BY:



Andrew M. Sarangan, Ph. D.  
Associate Professor  
Electro-Optics Program  
University of Dayton  
Committee Chairman



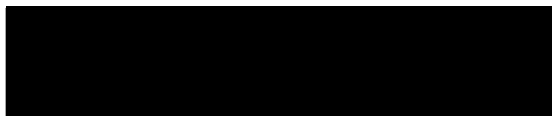
Joseph W. Haus, Ph. D.  
Professor and Director  
Electro-Optics Program  
University of Dayton  
Committee Member



Qiwen Zhan, Ph. D.  
Assistant Professor  
Electro-Optics Program  
University of Dayton  
Committee Member



Donald L. Moon, Ph. D.  
Associate Dean  
Graduate Engineering Programs  
and Research  
School of Engineering



Joseph E. Saliba, Ph. D., P.E.  
Dean, School of Engineering  
University of Dayton

## ABSTRACT

### THE DESIGN AND FABRICATION OF HIGH PERFORMANCE OPTICAL INTERFERENCE FILTERS FOR THE MID-INFRARED REGION

Fehrman, Emily Marie  
University of Dayton

Advisor: Dr. A. M. Sarangan

Optical interference filters are an essential component of many types of optical systems. Interference filters are multilayer thin film structures that operate on the principle of constructive and destructive interference of reflected optical waves from the high and low refractive index interfaces. Interference filters in the 3-5  $\mu\text{m}$  mid-infrared band have important applications in night vision and thermal imaging. In this thesis, a technique for designing and fabricating high-performance mid-infrared filters with a high degree of repeatability is presented. The filters in this study were fabricated using germanium and silicon dioxide. The designs were numerically optimized using the simplex and genetic algorithms, and were deposited using RF magnetron sputter deposition.

Since the performance of interference filters is significantly influenced by the accuracy of the refractive index of each film, the dispersion of the index of refraction of germanium and silicon dioxide were characterized in the 3 to 5  $\mu\text{m}$  region. Although the results from silicon dioxide films were consistent with others' results, germanium films

were found to have significantly higher refractive indices than commonly accepted values. It was concluded that the index of refraction of sputtered germanium is higher than that of bulk crystalline germanium. From Raman spectroscopy it was concluded that the sputtered germanium films are under tensile stress, and are either amorphous or polycrystalline in structure. From the energy dispersive X-ray spectroscopy, it was determined that the germanium films were not contaminated by argon or any other materials present in the sputtering chamber.

In addition to the refractive index, high-performance filters also require precise control of the film thicknesses. However, run to run variations in deposition rates are unavoidable, due to process fluctuations and target erosion. A dynamic, running-design process was developed where the design is re-optimized after each layer deposition such that the performance degradation due to errors from prior layers are partially recovered during the subsequent layers. This technique proved to be an effective means of maintaining filter spectral performance when the deposition thicknesses are not precisely controlled.

## ACKNOWLEDGEMENTS

I would like to thank Dr. Andrew Sarangan and Dr. Aziz Mafoud Familia for their profound help and guidance throughout this process. I would also like to thank Arun Mehadevan, Mengshu Pan, and Agus Widjaja for their assistance with fabrication. Many thanks to Scott Streiker of the University of Dayton Nanoscale Engineering Science and Technology Laboratory and to Dr. Mathias Schubert of the University of Nebraska-Lincoln Department of Electrical Engineering Nebraska Center for Materials and Nanoscience for their help and expertise. Finally, I would like to thank my parents, my brother, and Josh for their constant support and for their confidence in me.

## PREFACE

Optical interference filters are often thought of as periodic structures that can be easily fabricated. In reality, the periodic interference filter is a text book example used for illustration purposes only. To design a practical high performance optical filter, a sophisticated optimization algorithm is required. The resulting design will be a complex aperiodic structure with several dozen layers. The number of required layers can be reduced if a large contrast in refractive index exists between the two materials in the filter design. However, even the choice of materials becomes complex because what works for one wavelength band, such as the visible band, does not work for another band, such as the infrared band. The optical properties of the materials must be well understood in order to design and build a filter repeatably. This thesis will address the design and fabrication process for high-performance interference filters for the 3 to 5  $\mu\text{m}$  mid-infrared wavelength range. These types of filters can be used to spectrally resolve images for night vision or thermal imaging applications.

Germanium is an important material for the mid-infrared region because it has a very high index of refraction. While the index of refraction of bulk crystalline germanium is well defined, little is known about the specific optical properties of thin films produced by sputtering germanium. This thesis will address, as an integral part of the discussion on filter design and fabrication, the dispersion of the index of refraction of

germanium in the 3 to 5  $\mu\text{m}$  region and the impact of imprecise knowledge of the index of refraction and film thickness control on interference filter design and modeling.

## TABLE OF CONTENTS

ABSTRACT.....	iii
ACKNOWLEDGEMENTS.....	v
PREFACE.....	vi
CHAPTER	
I. BASIC FILTER APPLICATIONS AND DESIGNS.....	1
1.1 APPLICATIONS OF OPTICAL FILTERS .....	1
1.2 TYPES OF OPTICAL FILTERS .....	3
1.3 TRANSFER MATRIX METHOD FOR MODELING MULTILAYER FILTERS.....	6
1.4 PRACTICAL FILTER DESIGN.....	9
II. OVERVIEW OF THIN FILM DEPOSITION METHODS .....	14
2.1 INTRODUCTION TO THIN FILM DEPOSITION.....	14
2.1.1 Thin Film Deposition by Evaporation .....	14
2.1.2 Thin Film Deposition by Chemical Vapor Deposition.....	16
2.2 SPUTTER DEPOSITION .....	17
2.3 VACUUM SYSTEMS AND THE EFFECT OF VACUUM ON THIN FILM DEPOSITION .....	25
2.5 THICKNESS MONITORING DURING THIN FILM DEPOSITION .....	30
III. FILTER DESIGNS FOR THE MID-INFRARED (3-5 $\mu$ M) WAVELENGTH REGION .....	33
3.1 MID-INFRARED FILTER APPLICATIONS .....	33
3.2 DESIRED HIGH AND LOW PASS FILTER PERFORMANCE.....	33
3.3 FILMSTAR DESIGN SOFTWARE AND OPTIMIZATION ALGORITHMS.....	35
3.4 USER INTERVENTION DURING OPTIMIZATION .....	40
3.5 REAL TIME DESIGN OPTIMIZATION DURING FABRICATION .....	42
IV. ANALYSIS OF FABRICATED HIGH AND LOW PASS FILTER PERFORMANCE.....	46
4.1 TRANSMISSION SPECTRA OF SELECTED FILTERS .....	46
4.2 PHYSICAL AND OPTICAL PROPERTIES OF SPUTTERED GERMANIUM AND SILICON DIOXIDE FILMS .....	55
V. CONCLUSIONS.....	64
BIBLIOGRAPHY.....	68

## LIST OF FIGURES

1. Ideal band-pass (a) and band-stop (b) filters in the 3-5 $\mu\text{m}$ wavelength region.....	3
2. Ideal high- (a) and low-pass (b) edge filters, designed for the 3-5 $\mu\text{m}$ range, with a sharp transition at 4 $\mu\text{m}$ .....	4
3. Ideal band-pass filter created from high- and low-pass edge filters.....	5
4. Reflection and transmission at the layer boundary for TMM modeling.....	6
5. ABA filter structure.....	8
6. Example 3 layer ABA spike filter transmission performance in the 3-5 $\mu\text{m}$ wavelength region.....	9
7. A filter where films have begun to peel due to stress.....	12
8. Conformal vs. directional coatings.....	15
9. Two configurations for DC sputtering chambers. When the chamber walls serve as the anode, the plasma becomes weak near the substrate since the anode is larger than the cathode.....	18
10. Crooke's, Faraday's, and Anode dark spaces.....	19
11. Ion reflection, ion implantation, and sputtering.....	20
12. Positive and negative cycles in an RF sputtering system.....	22
13. DC bias in an RF sputtering system. [4].....	22
14. Magnet and magnetic field configuration for a magnetron cathode. [4].....	23
15. Characteristic erosion pattern on an $\text{SiO}_2$ magnetron sputtering target.....	23
16. RF Magnetron Sputter cathode without target installed.....	24
17. RF Magnetron Sputter cathode with target installed.....	24

18. Rotary vane pump. [3].....	27
19. Cross-section of a turbomolecular pump [5].....	28
20. Schematic of a molecular drag pump [8].....	29
21. Sputtering chamber, in use, with crystal monitor, rotation stage, and cathodes identified. Text added. [9].....	30
22. Thickness variation across a sputtered Ta <sub>2</sub> O <sub>5</sub> thin film.....	31
23. Measured performance of the high- and low-pass filters.....	34
24. Measured layer thickness for the high-pass (a) and low-pass (b) filters.....	34
25. High-pass filter targets and optimized design transmission plot from FilmStar. The green line is the desired target spectrum and the red line is the optimized value. [10]....	35
26. FilmStar film indices definition table. [10].....	36
27. Second side compensation options for FilmStar. FWD refers to the front surface of the substrate where the filter is built. Side 2 refers to the backside of the substrate which has a reflection that can either be included or ignored in the model. [10].....	36
28. Two-dimensional representation of the reflection, expansion and contraction moves in the simplex method. [11].....	38
29. FilmStar transmission plot showing the real time update of a high-pass filter during simplex optimization. [10].....	40
30. Comparison of a high-pass filter model transmission profile using only 3, 5, 11, and all 23 layers.....	42
31. Continual design re-optimization during fabrication.....	43
32. Model of the degradation of filter performance when the real-time design optimization process is not implemented.....	44
33. Model of how filter performance is preserved by the real-time design optimization process.....	44
34. The first high-pass filter attempt.....	46
35. Filter #2.....	47

36. Filter #3. First indication of the germanium index of refraction error.....	49
37. For a very flat, broadband filter, small variations of the index of refraction may not be apparent.....	50
38. Filter 10 FTIR measured performance compared to the model for the first 15 layers.....	51
39. Filter #10 FTIR measured performance compared to the model after the deposition of the final layer.....	51
40. Measured FTIR transmission compared to the FilmStar Model for two different values for the germanium index of refraction for low-pass filter #28 (a) and high-pass filter #29 (b).....	53
41. Raman spectra for bulk crystalline germanium and for a germanium thin film sputtered at 4 mTorr argon pressure and 180 Watts RF power.....	56
42. Energy dispersive X-ray (EDS) spectra of a single sputtered germanium thin film on a silicon substrate.....	58
43. Estimated dispersion in the real part of the index of refraction of sputtered germanium.....	60
44. Real (a) and imaginary (b) parts of the index of refraction of sputtered SiO <sub>2</sub> in the 3-5 $\mu$ m region from ellipsometry data.....	61
45. Real (a) and imaginary (b) parts of the index of refraction of sputtered germanium in the 3-5 $\mu$ m region from ellipsometry data.....	62
46. Filter #29 (a) and Filter #28 (b) FTIR transmission spectra compared to the FilmStar model using dispersion for Ge and SiO <sub>2</sub> .....	63
47. High performance low-pass filter fabricated using the real-time design optimization process. Wavelength in nm.....	65

## LIST OF TABLES

1. Raman spectroscopy results for single layer sputtered germanium films. Shift in characteristic peak and full width half max of peaks.....	56
--	----

## CHAPTER I

### Basic Filter Applications and Designs

#### 1.1 Applications of Optical Filters

Optical filters are used for a wide variety of applications for wavelengths ranging from the visible region to the infrared. An optical filter is a device designed to block or transmit selected wavelengths or a particular range of wavelengths. Filters are used in many common consumer products, but are also used in industrial and research settings.

A commonly used and relatively simple type of optical filter is an antireflection coating [1]. These can be found on eyeglasses, photographic lenses, and other optics where they minimize losses through reflection. Antireflection coatings are usually composed of just one or two thin films, and operate on the principle that reflections can be reduced by destructive interference. If the optical thickness (index of refraction multiplied by the physical thickness) of the applied film is one quarter of the wavelength in question, the reflections from the front and backside of the film will destructively interfere, eliminating the reflection. The simplest type antireflection coating uses a single film, usually with quarter-wavelength optical thickness. The index of refraction of the film is also important. For a film with one quarter-wavelength optical thickness on an air/substrate interface, the index of refraction of the film that will produce zero reflectance is equal to the square root of the index of refraction of the substrate. A

common material used for antireflection coatings on glass lenses for visible wavelengths is magnesium fluoride, which has an index of refraction of 1.38. This material is used even though it does not reduce the reflections to zero because it is a hard durable film that acts as a protective coating in addition to an antireflection coating. Other materials used for antireflection coatings, and for other optical filters, especially in the visible region are zinc sulfide ( $n=2.3$ ), silicon monoxide ( $n=1.86$ ), tantalum pentoxide ( $n=2.15$ ), lanthanum trifluoride ( $n=1.57$ ), cerium fluoride ( $n=1.60$ ), hafnium oxide ( $n=2.05$ ), and yttrium oxide ( $n=1.85$ ). For maximum reduction of reflection, multiple thin films can be applied to obtain a more effective destructive interference from the larger number of reflected waves.

The opposite of an antireflection coating is a high-reflection coating [1]. These can be thin, metallic films applied to polished glass substrates in order to form mirrors. Aluminum is the most common metallic film used in mirrors, but other metals such as gold, silver, rhodium and copper are also used. Multiple layers of dielectric materials with a high index of refraction can also be applied to a substrate to provide maximum constructive interference, which gives the surface a high reflectivity. Dielectric and metallic films can be used together or separately to create dichroic mirrors. Dichroic mirrors are used to control heat in optical devices. Hot mirrors reflect near infrared radiation and transmit the visible spectrum, while cold mirrors reflect the visible spectrum and pass the infrared.

Filters are used to isolate desired optical signals, such as a particular laser or spectral line, from ambient light. This idea can also be applied in digital color photography. An array of microfilters can be used on each light sensing pixel in a digital

camera to select out the portion of the total light signal corresponding to red, blue, yellow and green wavelength bands to produce the color image. This same configuration could be used with an array of infrared filters to create multi-spectral thermal images. Each filter in the array senses a different range of infrared wavelengths which corresponds to a different thermal signature.

### 1.2 Types of Optical Filters

There are several different types of optical filters, categorized by the shape and function of their transmission and reflection spectra [1]. The three main types of filters are band-pass, band-stop, and edge filters. Since the sum of the total reflection and transmission is unity, filters can be thought of in terms of either the reflection or transmission properties they present, depending on the use of the filter. This discussion will focus on the transmission properties of the various types of filters, but it is useful to remember that these same devices can be exploited for their reflective properties. Band-pass filters are designed to transmit, or pass, a defined range of wavelengths, and to reject all other wavelengths outside of the

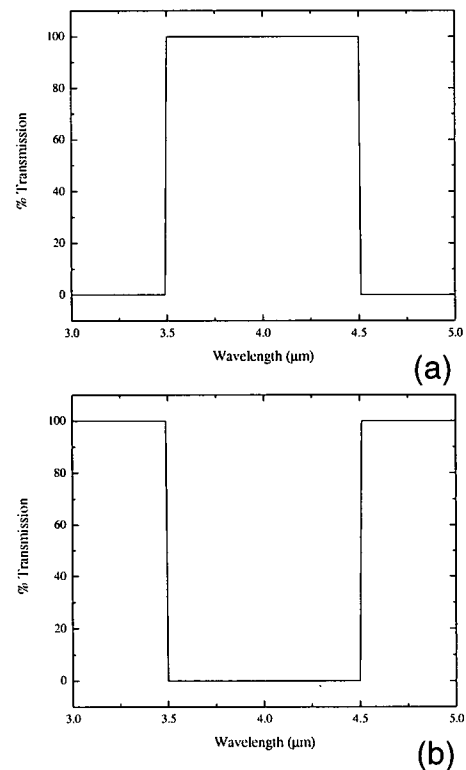


**Figure 1: Ideal band-pass (a) and band-stop (b) filters in the 3-5 μm wavelength region.**

defined range, as shown in Fig. 1-a. A narrow band-pass filter is often referred to as a

spike filter. A band-stop filter, also known as a notch filter, is the opposite of a band-pass filter. A band-stop filter attenuates a selected range of wavelengths and transmits all other wavelengths, as shown in Fig. 1-b. Often, the term notch filter is reserved for a band-stop filter that attenuates only a very small range of wavelengths. A band-pass or band-stop filter can be as broad or as narrow a defined wavelength region as necessary. An edge filter is designed to have a sharp transition from attenuation to transmission at a

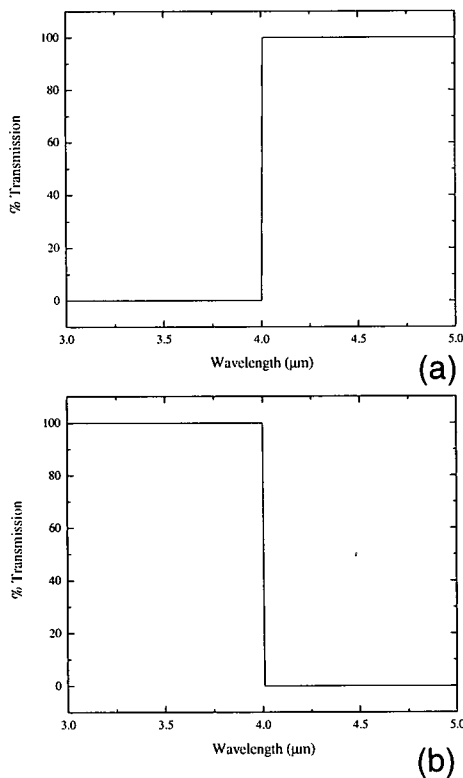


**Figure 2: Ideal high- (a) and low-pass (b) edge filters, designed for the 3-5  $\mu\text{m}$  range, with a sharp transition at 4  $\mu\text{m}$ .**

single wavelength, shown in Fig. 2. Edge filters are generally categorized as high-pass or low-pass. A high-pass, or long-pass, filter, as the name implies, passes long wavelengths and attenuates short wavelengths. A low-pass, or short-pass, filter does the opposite.

A pair of high- and low-pass filters, designed for different transition wavelengths, could be used together to create a band-pass filter or a band-stop filter, as shown in Fig. 3. Ideally, all three of these filter types perfectly transmit the selected wavelengths and perfectly attenuate the rejected wavelengths, in addition to having a perfect, immediate transition from

transmission to attenuation. However, this is never the case in practice, for reasons addressed later.

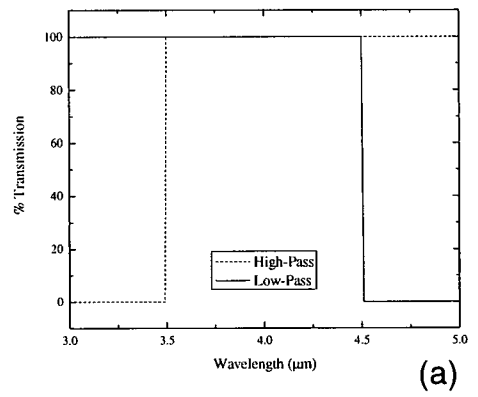


**Figure 3: Ideal band-pass filter created from high- and low-pass edge filters.**

### 1.3 Transfer Matrix Method for Modeling Multilayer Filters

While certain glasses and other bulk materials can be used alone as filters, the filtering capabilities of these materials are fixed by their natural properties and cannot be changed. Layering thin films of multiple materials allows filters to be tailored to particular applications. Filters made from layers of multiple thin films are based on constructive and destructive interference of the reflection and transmission at each layer interface. These interference effects can be modeled with the transfer matrix method (TMM) [2].

Fig. 4 shows the forward and backward traveling fields at several layer boundaries. The thicknesses of each layer are described by  $z$ , the distance traveled into the filter from the

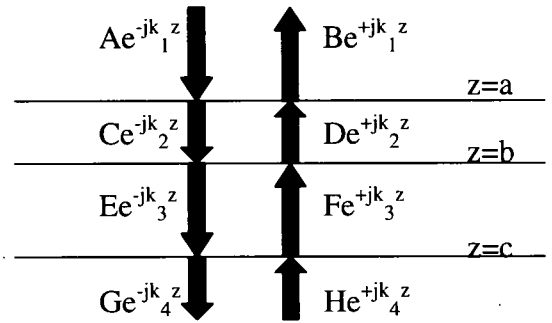


**Figure 4: Reflection and transmission at the layer boundary for TMM modeling.**

surface,  $z=0$ . The index of refraction of each layer is embedded in the number  $k_x$ , where

$$k_x = \frac{2\pi n_x}{\lambda} \quad (1)$$

and  $\lambda$  is the wavelength of the incident light. The field amplitudes and their derivatives must be continuous across each boundary, therefore at the first boundary ( $z=a$ ),

$$\begin{bmatrix} e^{-jk_1 a} & e^{+jk_1 a} \\ -jk_1 e^{-jk_1 a} & +jk_1 e^{+jk_1 a} \end{bmatrix} \begin{bmatrix} A \\ B \end{bmatrix} = \begin{bmatrix} e^{-jk_2 a} & e^{+jk_2 a} \\ -jk_2 e^{-jk_2 a} & +jk_2 e^{+jk_2 a} \end{bmatrix} \begin{bmatrix} C \\ D \end{bmatrix}. \quad (2)$$

Similarly, at the second boundary ( $z=b$ ),

$$\begin{bmatrix} e^{-jk_2 b} & e^{+jk_2 b} \\ -jk_2 e^{-jk_2 b} & +jk_2 e^{+jk_2 b} \end{bmatrix} \begin{bmatrix} C \\ D \end{bmatrix} = \begin{bmatrix} e^{-jk_3 b} & e^{+jk_3 b} \\ -jk_3 e^{-jk_3 b} & +jk_3 e^{+jk_3 b} \end{bmatrix} \begin{bmatrix} E \\ F \end{bmatrix}. \quad (3)$$

If  $M_n(z)$  is defined as

$$M_n(z) = \begin{bmatrix} e^{-jk_n z} & e^{+jk_n z} \\ -jk_n e^{-jk_n z} & +jk_n e^{+jk_n z} \end{bmatrix}, \quad (4)$$

substituting this into equations (2) and (3) gives,

$$\begin{aligned} M_1(a) \begin{bmatrix} A \\ B \end{bmatrix} &= M_2(a) \begin{bmatrix} C \\ D \end{bmatrix} \\ M_2(b) \begin{bmatrix} C \\ D \end{bmatrix} &= M_3(b) \begin{bmatrix} E \\ F \end{bmatrix}. \end{aligned} \quad (5)$$

Manipulation of these equations lead to the final result of

$$M_3^{-1}(b)M_2(b)M_2^{-1}(a)M_1(a) \begin{bmatrix} A \\ B \end{bmatrix} = \begin{bmatrix} E \\ F \end{bmatrix}. \quad (6)$$

For a structure composed of N layers, with Y and Z as the field amplitudes of the last layers of the structure, this equation (6) can be generalized to

$$M_N^{-1}(z_N)M_{N-1}(z_N).....M_3^{-1}(b)M_2(b)M_2^{-1}(a)M_1(a) \begin{bmatrix} A \\ B \end{bmatrix} = \begin{bmatrix} Y \\ Z \end{bmatrix}. \quad (7)$$

Equation (7) can be simplified by defining the transfer matrix T, as

$$T = M_N^{-1}(z_N)M_{N-1}(z_N).....M_3^{-1}(b)M_2(b)M_2^{-1}(a)M_1(a) \quad (8)$$

so that

$$T \begin{bmatrix} A \\ B \end{bmatrix} = \begin{bmatrix} Y \\ Z \end{bmatrix}. \quad (9)$$

Since the wave reflected back into the structure from external components is zero, for an incident field with an amplitude of one, equation (9) can be rewritten in terms of the field reflection and transmission coefficients, r and t.

$$T \begin{bmatrix} 1 \\ r \end{bmatrix} = \begin{bmatrix} t \\ 0 \end{bmatrix}. \quad (10)$$

From this, we can derive equations for the reflection and transmission coefficients for the structure at a particular wavelength.

$$r = -\frac{T_{21}}{T_{22}}$$

$$t = T_{11} - \frac{T_{12}T_{21}}{T_{22}} = T_{11} + T_{12}r \quad (11)$$

For a given structure, the transfer matrix can be evaluated as a function of wavelength and the transmission or reflection spectra can be plotted. The textbook

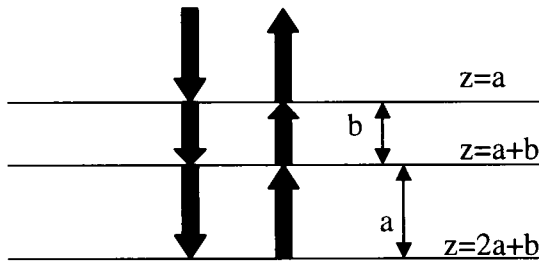


**Figure 5: ABA filter structure.**

example for a filter structure is the ABA model. This is a filter designed with two materials, one of high index of refraction, and one of low index of refraction, in alternating layers. All layers of the low index material have

thickness A, and all layers of the high index material have thickness B, where A and B are not necessarily the same thickness. Fig. 5 shows an example three layer ABA structure. It is important to remember that  $r$  and  $t$  are both functions of wavelength, which is embedded in  $k$ , as shown in equation (1). Assuming that in the 3 layer ABA structure material A has an index of refraction of  $n_A=1.5$ , and thickness  $a=1.33 \mu\text{m}$ , and material B has an index of refraction  $n_B=4.5$  and thickness  $b=0.89 \mu\text{m}$ , the transmission profile of this structure, over the 3 to 5  $\mu\text{m}$  wavelength range, will be as shown in Fig. 6. This filter has a peak transmission at 4  $\mu\text{m}$  and lower transmission elsewhere. The performance of this filter might be acceptable depending on the application, even though the attenuation is weak and the transmission peak is not sharp.

Although TMM is a powerful technique for predicting the spectral performance for a given structure, in most practical situations the designer is required to come up with

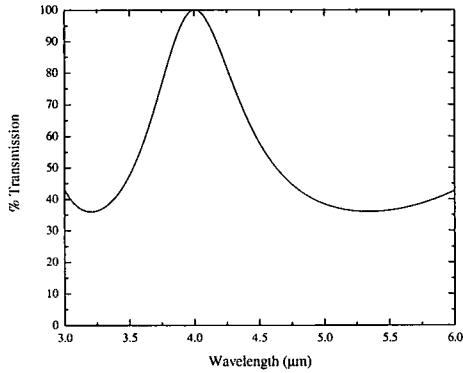


**Figure 6: Example 3 layer ABA spike filter transmission performance in the 3-5  $\mu\text{m}$  wavelength region.**

the layer structure to meet a given spectral performance. It is impractical to derive an inverse-TMM formulation that analytically relates the target spectral performance to a layer structure. In order to create a filter design to meet a target performance, an

optimization routine is required. This routine iteratively applies the TMM. The routine starts with an initial design, calculates the

transmission of the design for the desired wavelengths, and then compares the performance with the target performance. Based on the difference between the target and calculated spectral performance, an error function is generated. The error function is used to modify the layer structure, and the process repeats. This optimization routine loops until the error between the target and calculated performance becomes acceptable, based on numerous factors. The optimization process is the subject of Chapter 3.

#### 1.4 Practical Filter Design

While the transfer matrix method described in the previous section is used for predicting the spectral performance of a known structure, it cannot be used in the existing form for designing a structure. It is not practical to begin with the desired spectral performance and attempt to back calculate the layer thicknesses using the TMM. This is

a tedious process to do by hand, especially if guess-and-check methods are used to modify the structure. Instead, a more complex, systematic algorithm should be employed to optimize the structure.

The filter designs obtained from the optimization are rarely periodic ABA structures, like those discussed in section 1.3. Instead, the layer thicknesses are generally aperiodic. From the fabrication perspective, an aperiodic stack is not any more complicated than a periodic stack. Since each layer has to be deposited one by one, they can have arbitrary thicknesses. Deposition difficulties are usually related to other factors such as number of layer transitions and total thicknesses, as will be discussed in chapter 2. The periodic ABA filter structure is really just a text book example used to demonstrate the TMM because it allows for simplification of the matrices. Although typical filters utilize just two alternating materials, three or more materials can also be used, resulting in a structure that is aperiodic not only in its layer thicknesses, but also in its refractive indices. This may give the designer additional flexibility to achieve the target performance. However, such filters are rarely made because larger number of materials typically poses additional challenges for deposition.

Before designing a multilayer optical filter, several parameters must be considered and specified. The first step is to define the desired spectral output of the filter and the intended use for the filter. Once this is defined, suitable materials for fabrication can be identified. Materials should be chosen based on the index of refraction and dispersion over the required wavelength range, availability, compatibility with available or desired deposition methods, and should be durable enough to withstand the conditions under which the final product will be used. Details of fabrication are covered

in chapter 3. The next step is to experimentally determine the index of refraction or dispersion of the chosen materials for the appropriate wavelengths. An accurate index of refraction is essential to a successful model of the filter's performance. The materials should have a high index contrast whenever possible. A high index contrast produces larger reflections at the layer interfaces. These larger reflections allow the filter to achieve the desired performance with fewer layers than would be necessary with a smaller index contrast. However, it is not always possible to have a high index contrast, because a high index contrast requires the deposited layers to have high quality and low surface roughness. This is because any defects at the interface will produce strong scattering when the index contrast is high. The surface roughness and film quality will depend on the deposition method used.

The maximum number of layers, total filter thickness limits, and individual layer thickness limits must be defined. These parameters will be determined by several interrelated factors. First, the more layers that are added to the filter, the sharper the filter performance will be due to the larger number of interfering waves. If the filter is designed to have a sharp transition, such as an edge filter, twenty or more layers may be required. However, for broadband applications, such as AR coatings, one or two layers may be acceptable. A greater total thickness may be required for sharp edge filters, in order to accommodate the greater number of layers. Individual layer thickness must also be considered. Limits may be placed on the individual thickness limits based on the available thickness measurement techniques and the time required to deposit each layer.

However, there are several practical concerns when determining the thickness parameters and number of layers for a filter. The first consideration is deposition time.

The deposition rates of the chosen materials and the time it takes just to prepare the vacuum chamber and operate the deposition tool will determine how long it will take to deposit one layer of the chosen materials. If one or both of the materials have a slow deposition rate, it may be decided to limit the thicknesses of some or all layers so that the filter can be grown in a reasonable amount of time. Second, if the filter will undergo etching or lift-off processes after fabrication, the thickness of each layer, and possibly the number of layers, will need to be limited in order to limit the total thickness of the filter. Lift-off becomes difficult for total thicknesses greater than about 5  $\mu\text{m}$ , so this could be a limiting factor in the filter design. Third, stress occurs in the films as they are deposited



**Figure 7: A filter where films have begun to peel due to stress.**

due to varying thermal expansion of the films. Stress will also vary depending on the deposition method used, but in general, stress increases with thickness. Very thin films may be able to adapt and conform to the substrate, while thicker films will tend to acquire their bulk properties, and if it is different from the substrate, significant

stresses can accumulate. Consideration must be given to the operating temperature of the filter. If the filter will be used at cryogenic temperatures, additional stress can build during the cool-down and warm-up cycles. If stress has been observed in films of a certain thickness, this should be considered when setting the layer thickness limits. Large amounts of stress can cause thin films to peel away from the substrate and other films, destroying the filter, as shown in Fig. 7. Finally, the method for monitoring the film

thickness during deposition must be considered. This topic will be discussed more thoroughly in section 2.5, but depending on the method used, a lower or upper limit to individual layer or total thickness may be determined by the limitations of the monitoring method.

## CHAPTER II

### Overview of Thin Film Deposition Methods

#### 2.1 Introduction to Thin Film Deposition

The three commonly used types of deposition systems are sputtering, evaporation, and chemical vapor deposition (CVD). The filters fabricated for this thesis were grown by sputtering, so only a brief overview of evaporation and chemical vapor deposition will be given in this section for completeness. A more thorough description of sputtering will be given in section 2.2. All of these deposition methods are performed under vacuum. Vacuum systems and the purpose of vacuum in thin film deposition will be described in section 2.3. Finally, the monitoring and measurement of deposited film thickness will be the subject of section 2.4.

##### 2.1.1 Thin Film Deposition by Evaporation

Evaporation is a very simple method for depositing thin films [3], [4]. The source material is placed in a crucible and heated until it becomes molten. The vapor pressure of the source will increase with increasing temperature, approaching very high values as the source nears its melting point. If a substrate is placed above the molten material, the vapor will condense on the substrate, much like water condensing on a cold surface on a humid day. Evaporation must be done under high vacuum. Higher deposition pressures

can lead to contamination and lower deposition rates. The elevated temperature will make the evaporating species highly reactive with the background gases and may create oxides or nitrides in the resulting film. Furthermore, higher pressures will cause the evaporated molecules to collide with the

background gases, causing them to be scattered in random directions. This can

lower the deposition rate, because much of the vapor will condense on random surfaces instead of on the substrate. In the  $\mu\text{Torr}$

range, the mean-free path will become long

enough to assume that the material leaving the molten material travels in a straight line.

As a result, the film will be highly directional, adhering only on surfaces that are in direct line of sight with the molten source. This feature makes evaporation very useful for

creating lift-off structures using photoresist masking. In addition, the evaporated atoms have relatively low energy, compared to sputtering, as will be discussed in section 2.2.

As a result, they have little mobility once they reach the surface of the substrate, which further improving the directionality. Fig. 8 illustrates the conformal and directional

depositions.

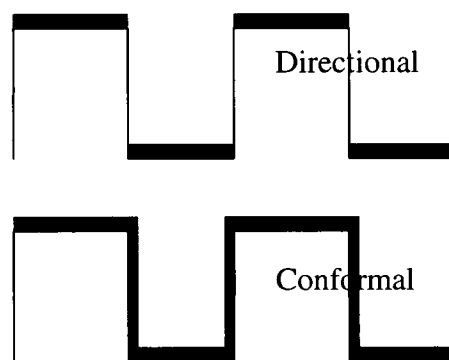


**Figure 8: Conformal vs. directional coatings.**

Three common types of crucible heating systems are resistive, inductive, and electron-beam. Resistive and inductive heating systems are simple and relatively inexpensive, but suffer from contamination problems. In a resistive system, since heat is applied by a filament from below the crucible, the filament and crucible can also evaporate in addition to the source, causing contamination. In an inductive system a wire

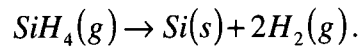
coil is used to induce eddy currents in the material in the crucible, causing it to heat. In this case, the wire itself can be cooled to prevent it from evaporating, but there is still no way to prevent the crucible from becoming hot and contaminating the material. Electron beam evaporation solves many of these problems. In an electron beam system, a high energy beam of electrons is directed at the surface of the material avoiding excessive heating of the crucible. This limits the heating to the desired material only, preventing contamination.

Evaporation is commonly used for single-element metals and in some limited cases for very stable compound dielectrics such as  $\text{SiO}_2$ . This process is not suitable for most compounds. When compounds are evaporated, they can dissociate into its constituent atoms due to the high temperature. Since the individual vapor pressures are likely to be different, evaporation rates of each component will be different. For this reason, the composition of the deposited film can be different from the composition of the bulk material.

### 2.1.2 Thin Film Deposition by Chemical Vapor Deposition

In a chemical vapor deposition system, thin films are created on the substrate by means of chemical reactions between gases. The gases needed for the reaction, called precursors, are pumped into a reactor chamber that contains the substrate. The precursors combine in the reactor, and the desired film material precipitates out of the gas mixture and coats the substrate, and any byproducts are pumped out of the reactor. A common reaction used in CVD is the decomposition of silane gas to form polycrystalline silicon

(p-Si) thin films. This reaction is simple in that it requires only one gas and the application of heat to decompose the silane. The reaction that occurs is



In this reaction, as the silane decomposes, the polycrystalline silicon condenses on the substrate, and the byproduct hydrogen is pumped out of the chamber. The reactions used in CVD can only produce a limited number of thin film materials, the most common being silicon, silicon oxides, and silicon nitrides.

CVD reactions require the addition of energy to break up the precursors into volatile radicals. The temperatures required to achieve this are not always practical to reach through conventional heating methods. Instead, the high energy ions from a plasma discharge are often used to break the bonds of the precursor molecules to allow the reaction to occur. The use of a plasma in a CVD system is called a Plasma Enhanced Chemical Vapor Deposition, or PECVD system.

Films produced through CVD are very conformal, hard and non-porous. Contamination is also a problem for CVD films. If the byproducts of the reaction are not efficiently pumped out of the reactor, these materials could also become a source of contamination. CVD is usually performed under vacuum to minimize contamination and to sustain a plasma, although atmospheric CVD is also possible.

## 2.2 Sputter Deposition

Sputtering was the method used to fabricate the interference filters in this thesis. Sputtering is a physical deposition that uses high energy ions in a plasma discharge to dislodge atoms from a bulk material, called the target [3], [4]. These dislodged atoms are

ejected (sputtered) away from the target towards the substrate, where the atoms collect to form a thin film. In this section, sputtering will be discussed beginning with the simplest method, DC sputtering, and moving to the progressively more complex methods of RF and magnetron sputtering.

In a direct current (DC) sputtering system, an argon plasma is ignited between the cathode and the anode, as shown in Fig. 9. A plasma is a fluid of ionized atoms. When the electric field between the cathode and anode is high enough, the argon gas between them will break down, releasing free electrons and ions. The breakdown voltage ( $V_b$ ) required is dependent on the argon pressure ( $P$ ) and the distance between the cathode and anode ( $L$ ), as given by Paschen's Law.

$$V_b = B \frac{PL}{\log(PL) + b}$$

The free electrons created by the breakdown of the argon will be accelerated towards and absorbed by the anode, and the positive argon ions will be accelerated towards the

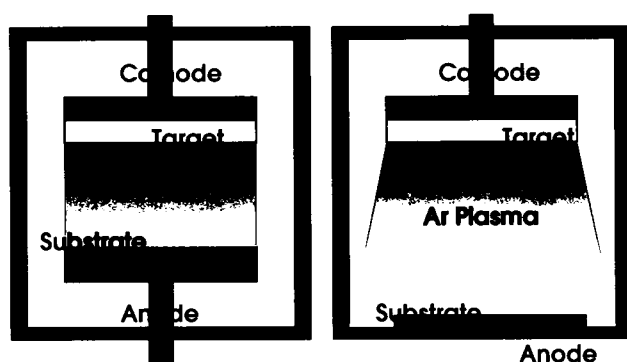


**Figure 9: Two configurations for DC sputtering chambers. When the chamber walls serve as the anode, the plasma becomes weak near the substrate since the anode is larger than the cathode.**

cathode. Argon ions are about 70,000 times more massive than electrons, and because they move so much more slowly, they can be considered stationary. Once all the electrons are absorbed at the anode, the current flow will stop and the plasma will extinguish

unless more electrons are supplied. However, if some of the argon ions near the cathode

have energy greater than the work function of the cathode material, they will release a secondary electron when they strike the cathode. These secondary electrons can then flow to the anode, continuing the current. As the electrons accelerate towards the anode, some of them will collide inelastically with neutral argon atoms, ionizing them. These new ions strike the cathode, causing the release of more secondary electrons. In this way, the plasma is sustained.

The argon plasma will display a characteristic purple glow discharge between the cathode and anode. When an electron collides inelastically with a neutral argon atom, but does not have enough energy to ionize that atom, it can excite core electrons in the argon atom to an excited state. As these excited atoms relax back down to the ground state, they emit photons, producing the characteristic plasma glow discharge. This emission process, fueled by secondary electrons, will occur throughout the plasma, with the



**Figure 10: Crooke's, Faraday's, and Anode dark spaces.**

exception of three dark spaces that occur in the plasma, as shown in Fig. 10. The region right next to the surface of the cathode, called the Crooke's dark space, will be dark because in this region the electron energy is too low to excite neutral argon atoms to emit photons. The

Faraday dark space occurs near the cathode. In this region, the accelerating electrons have reached high energies and all the collisions between electrons and neutral argon atoms in this region lead to ionization, not photon emission. The final dark space, called the anode dark space, occurs next to the anode. In this region, the electron density is low

because the electrons are being captured by the anode. There is little probability of electron-argon atom collisions in this region.

In addition to releasing secondary electrons, there are several other processes that can occur when an ion strikes the cathode, as shown in Fig. 11. If the ion has low energy, it may simply reflect off the cathode. If the ion has an energy greater than approximately 10 keV, the ion will penetrate into the cathode, several atomic layers deep. This is called ion implantation. For ions with energies between about 10 eV and 10 keV, some of the ion energy is transferred to the cathode as heat, and the rest of the energy causes atoms or atomic clusters to break free of the cathode. It is this mechanism that is referred to as sputtering. Approximately 95% of sputtered material is atomic, with the majority of the

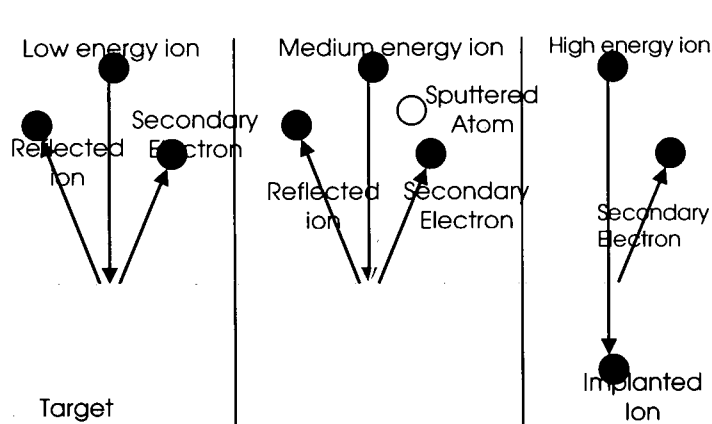


**Figure 11: Ion reflection, ion implantation, and sputtering.**

remainder being diatomic molecules.

If the target is a conducting material, the sputtering process proceeds as described above. The sputtered material is propelled towards the

substrate, forming a thin film. On average, the energy of a sputtered atom is 100 times greater than that of an evaporated atom. For this reason, sputtered atoms have a greater mobility at the substrate surface, and tend to naturally produce more conformal films than those produced by evaporation.

The argon pressure inside the sputtering chamber also impacts the directionality of the thin films. At a low argon pressure, the sputtered atoms will be less likely to collide with the gas atoms before hitting the substrate. In this case, the sputtered atoms will travel in a straight line path from the target to the substrate, which gives a highly directional film coating. At a high argon pressure, it is highly likely that the sputtered atoms will collide with another atom before hitting the substrate. At high pressure, the sputtered atoms will travel in a random path from the target to the substrate. This random motion of the sputtered atoms leads to a conformal film coating. The desired directionality of the sputtered film, depending on the specific application, can be achieved by controlling the argon pressure. However, arbitrary control of gas pressure is not possible because the plasma can only be sustained over a narrow range of pressure.

The DC sputtering process described above assumed a conducting target material that acts as an extension of the cathode itself. However, if the target material is insulating, such as  $\text{SiO}_2$ , a problem arises. As positive ions implant into the surface of the target, and secondary electrons are released, the exposed surface of the target gains a positive charge. The backside of the target, which is constantly fed by electrons through contact with the cathode, gains a negative charge. As this process continues, the voltage, and hence electric field, across the target will increase. This leads to a decrease in the electric field across the plasma. Eventually, the electric field will diminish so much as to extinguish the plasma, terminating the sputtering process. The solution to this problem is to use alternating current instead of direct current.

Radio Frequency (RF) sputtering uses alternating current to maintain the plasma even when insulating targets are used. In an RF system, an insulating target acts as a

capacitor in front of the cathode. During each cycle, the target will charge and discharge. If the frequency is high enough, the charging and discharging occurs fast enough to

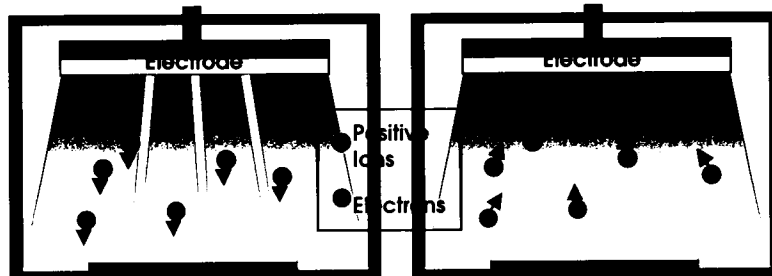


**Figure 12: Positive and negative cycles in an RF sputtering system.**

prevent the voltage across the target from increasing to the point where the plasma will extinguish. In an RF system, the sputtering

chamber is designed to have a single powered electrode and the chamber walls are set to ground to act as the second electrode. As is illustrated in Fig. 12, when the powered electrode is negative, sputtering occurs from the target.

However, when the powered electrode is positive, as is also illustrated in Fig. 12, the current flow can be sustained from stored electrons in the plasma. As long as the

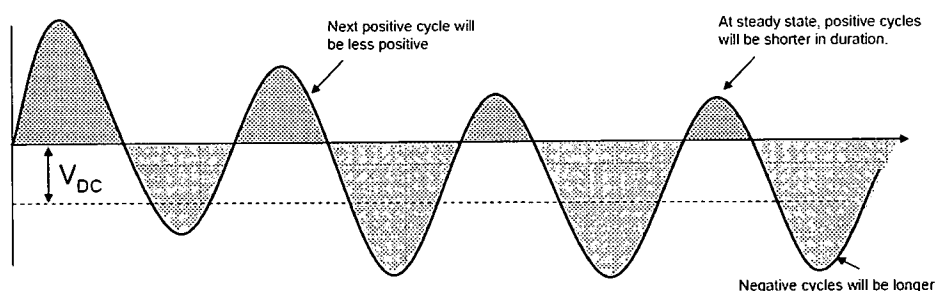


**Figure 13: DC bias in an RF sputtering system. [4]**

frequency is above 100 kHz and the plasma has a large volume, the electrode will draw

electrons from the plasma to sustain the current during the positive cycle. Because the time during which the electrode is positive is short enough so as not to deplete the supply of electrons in the plasma, ion bombardment on the negative chamber walls is not needed

to supplement the flow of electrons. The Federal Communications Commission (FCC) has assigned a frequency of 13.56 MHz for RF plasmas.

In an RF sputtering system, the RF generator is coupled to the electrode by means of a DC blocking capacitor. The RF signal will acquire a DC bias because electrons will be captured by the anode faster than secondary electrons can be released through ion

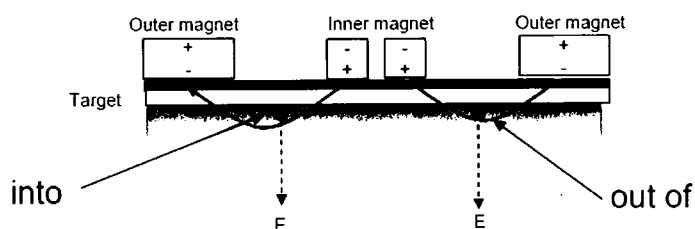


**Figure 14: Magnet and magnetic field configuration for a magnetron cathode. [4]**

bombardment. For this reason, a negative charge will build on the electrode side of the DC blocking capacitor during the first few RF cycles, adding a negative bias to the RF signal. After a few cycles, a steady state will be reached, where the positive cycles will be shorter than the negative cycles, as shown in Fig. 13. The magnitude of DC bias depends on the plasma characteristics, the mobility of electron and the rate of secondary electron emission. Generally, DC bias decreases with an increase in argon gas pressure, but increases with larger RF power, since it results in a larger voltage amplitude. If the DC bias is large, the negative cycle is longer. Since sputtering occurs during the negative cycle, a higher DC bias means a higher sputtering rate.

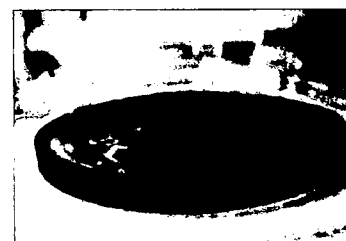


**Figure 15: Characteristic erosion pattern on an SiO<sub>2</sub> magnetron sputtering target.**

When secondary electrons are released, they drift in random directions and many simply exit the plasma and do not produce new ions. In magnetron sputtering, a

magnetic field is used to reign in the secondary electrons, pulling them close to the target surface. Two concentric ring magnets with opposite polarity are integrated into the target cathode, as shown in Fig. 14. The magnetic field created by this magnet configuration causes the secondary electrons to travel in a circular path around the target surface. This



**Figure 16: RF Magnetron Sputter cathode without target installed.**

increases the electron density at the target surface, creating a higher probability of electron-neutral atom collisions, so the number of ions created is increased. When the ion density increases, the sputtering rate increases because more ions collide with the target. Because the electrons are confined to a circular path around the target surface, the ion creation, and therefore sputtering, all happen in this circular track. This

leads to uneven erosion of the sputtering target, leaving a characteristic ring pattern in the target, as seen in Fig. 15.

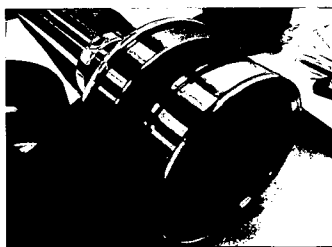


**Figure 17: RF Magnetron Sputter cathode with target installed.**

The magnetron cathode (manufactured by Angstrom Sciences), shown in Fig. 16, is water cooled, and has a copper plate which serves as the electrode. The ring magnets are located directly behind the copper plate. The target is mounted to this copper plate by means of a clamp ring, as shown in Fig. 17. If the target is insulating, conductive silver paste may be used to give better electrical and thermal contact between the target and the copper plate of the cathode.

Since sputtered films are created by simply letting the ejected atoms and molecules fall randomly onto the substrate, films created from crystalline targets will be

polycrystalline or amorphous. These films tend to also be porous and often show signs of stress, such as poor adhesion. Stress and porosity can be counteracted by heating the substrate. When the substrate is heated, the additional energy provided to the film atoms allows the atoms to pack more densely together, creating a less porous, harder film. Heating the substrate will also make the films more conformal, since the film atoms will be more mobile on the substrate surface. The chamber used for this work did not utilize a heated substrate stage.

Metals, dielectrics, and semiconductors can all be deposited by sputtering. Sputtering is also suitable for depositing complex compounds. Since the sputtering target is bombarded by energetic ions, all elements within the compound are equally likely to be ejected from the material, leading to the sputtered film having essentially the same composition as the sputter target. Materials that are very hard will have lower deposition rates than softer materials because it will take more energetic ions to break the atomic bonds. Magnetic materials, such as nickel, cannot be sputtered by magnetron sputtering because these materials will block the magnetic field.

### 2.3 Vacuum Systems and the effect of Vacuum on Thin Film Deposition

Sputtering, evaporation, and CVD are all performed under vacuum [3], [4]. Sputtering targets are usually manufactured to a high level of purity, usually 99.99% or better. The deposited film purity is largely controlled by the environment in which the films are deposited. Each time the deposition chamber is vented and opened, it is exposed to ambient air. Air is mostly nitrogen and oxygen, but also contains other trace gasses and water vapor. Small amounts of these gases will remain inside the chamber

even after vacuum pumping. As the sputtered atoms fall onto the substrate, these background gases can be trapped inside the thin film. This contamination could lead to variation in the index of refraction of the film as well as decreased adhesion to the substrate or durability of the film. It is therefore important to reach a very low pressure in the chamber prior to starting deposition, which is known as the ultimate base pressure of the system. The lower the base pressure, the higher the purity of the deposited film. When the material to be sputtered has a high deposition rate, a low base pressure may not be necessary because the sputtered atoms will hit the substrate faster than the time it takes for the background gases to meander onto the substrate. The materials used for this project have relatively low deposition rates, so to achieve a high level of purity in the deposited films a low base pressure, around  $7 \times 10^{-7}$  Torr was required. Very thin films sputtered at low rates at a high base pressure could exhibit significant contamination resulting in a noticeable difference in index of refraction or significant peeling of the film from the substrate. The deposition chamber should be kept under vacuum when not in use to prevent the build up of contaminants in the chamber over time. On larger production systems, the deposition chamber is under permanent vacuum and samples are inserted and removed through a load lock system.

The deposition system used for this work is the Denton Vacuum Explorer 14 magnetron sputtering system. It achieves vacuum through use of a rotary vane roughing pump and a turbomolecular drag pump. The rotary vane pump operates in the viscous gas flow regime, while the turbomolecular drag pump operates in the molecular gas flow regime. When the sputtering chamber is at atmospheric pressure, there are a large number of gas molecules inside the chamber. This is the viscous flow regime, where the

gas molecules constantly collide with each other. When molecules are removed from one end of the chamber by the mechanical pump, the large number of molecule collisions causes the pressure inside the chamber to immediately equalize. In other words, in the viscous flow regime, the pressure differential created by the mechanical pump is sufficient to cause molecules to flow into the pump.

One of the most common types of roughing pumps is the rotary vane pump [3],

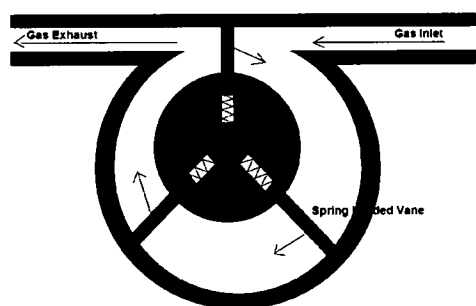


**Figure 18: Rotary vane pump. [3]**

[4]. The Denton Vacuum Explorer 14 magnetron sputtering system uses a dual stage rotary vane pump as the roughing pump. In a rotary vane pump (Fig. 18) an electric motor rotates an off-center metal cylinder inside of a cylindrical chamber. Several spring loaded vanes are attached to the rotating cylinder. As

the cylinder rotates, the vanes sweep along the inside wall of the chamber, sealing and unsealing different areas of the pump. Gas from the sputtering chamber becomes trapped by the rotating vanes, and since the axis of rotation for the vanes is off center, the gas becomes compressed as the compartment created by the rotating vanes becomes smaller and smaller. The compressed gas is then ejected at the high pressure exhaust port, or in a dual stage pump, travels to a second rotary vane pump.

However, the mechanical pump only works while the chamber remains in the viscous regime, whose lower limit is typically around 10 mTorr. Once the number of molecules in the chamber drops low enough that the remaining molecules have a higher probability of striking the chamber walls instead of each other, the gas flow has entered

the molecular regime. At this point, the turbomolecular drag pump must be engaged to bring the base pressure down to the required  $7 \times 10^{-7}$  Torr. In the molecular regime, the gas flow is entirely due to the motion of the individual molecules in the chamber. Unlike in the viscous regime, a simple pressure differential is not enough to cause gas flow out of the chamber. A more sophisticated pumping mechanism must be employed.

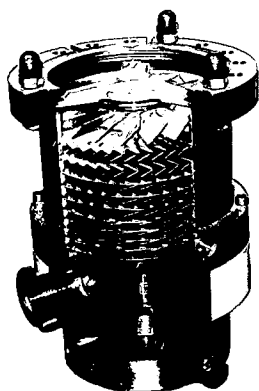


**Figure 19: Cross-section of a turbomolecular pump [5].**

A turbomolecular pump consists of several rotating fans in series [3], [4]. The tilt angle of the fan blades becomes progressively larger from the exhaust (high pressure) end to the inlet (low pressure) end, as shown in Fig. 18. Unlike the rotary vane pump, the turbomolecular pump is not designed to pull molecules out of the sputtering chamber. Instead, the turbomolecular pump traps any molecules that enter the pump inlet. The spinning fan blades are moving as fast as the speed of the molecules at the inlet, so when a molecule strikes one of these fan blades, a large downward velocity is imparted to the molecule. The molecule then passes to the next fan, where it gains another downward component to its velocity. The spacing between fans becomes smaller as the molecules move from the inlet to the exhaust, thus compressing the trapped gas molecules. Finally, the trapped molecules reach the high pressure exhaust, where they are expelled.

In the viscous regime, the composition of the gas inside the chamber remains uniform. The gas in the chamber consists of nitrogen, water vapor, oxygen, hydrogen, and other trace gases normally found in air. In the molecular regime, the gas composition changes. At pressures below 1 mTorr, the pressure will be largely due to water vapor. A

liquid nitrogen trap at the turbomolecular pump inlet removes much of the water vapor by condensing it. Below 0.1  $\mu$ Torr, hydrogen becomes the dominant gas. The fans inside a turbomolecular pump spin at extremely high speeds, usually greater than 20,000 rpm. A four inch turbomolecular pump spinning at 60,000 rpm will have an average blade speed of 160 meters per second. This is about 10 percent of the speed of a  $H_2$  molecule, not nearly enough for the turbomolecular pump to impart a significant downward velocity to trap the molecule. For this reason, even after the sputtering chamber is pumped by the turbomolecular pump, the chamber will still contain light, fast moving gasses, such as

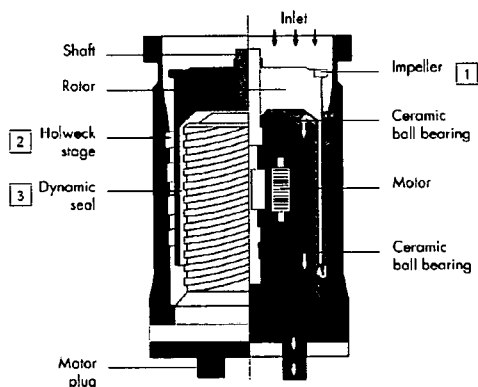


**Figure 20: Schematic of a molecular drag pump [8].**

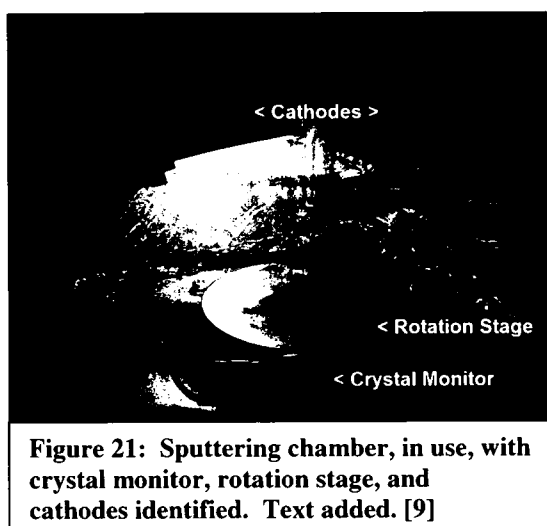
hydrogen and helium, which are nearly impossible to remove. Care must be taken not to expose a turbomolecular pump to high pressure at the inlet. A high inlet pressure can cause permanent damage to the rotating fans.

The high vacuum pump used in the Denton Vacuum Explorer 14 is a turbomolecular drag pump. A turbomolecular drag pump is a hybrid pump combining a turbomolecular pump and a molecular drag pump [4], [6], [7]. A molecular drag pump consists of a cylindrical rotor moving inside a helical stator, which drags the gas molecules in the same direction as the rotation of the pump (see Fig. 20). This is the opposite of what happens in a turbomolecular pump. In a turbomolecular pump, the rotating blades force the gas to move perpendicular to the rotation plane of the fans. Molecular pumps have the advantage of being able to operate at higher inlet pressures

than a turbomolecular pump, but has a slower pumping rate than the turbomolecular pump. In a hybrid pump, the molecular drag portion of the pump will engage first, lowering the pressure to an acceptable level for the turbomolecular pump, reducing the load on the turbomolecular pump.

## 2.5 Thickness Monitoring during Thin Film Deposition

Two main methods were employed to monitor the thickness of the deposited films. A crystal monitor was originally used to monitor the thickness during the deposition process, but later a companion piece was used to simply measure the physical



thickness of a film after each deposition step.

Each of these methods has its strengths and weaknesses, as will be discussed in this section.

The crystal thickness monitor is an oscillating quartz crystal, whose frequency varies with mass [1]. If such a crystal is placed inside the deposition chamber, near

the substrate, sputtered material will be deposited on the crystal as well as the substrate. As the sputtered film builds on top of the crystal, the crystal oscillation frequency changes. The change in oscillation can then be calibrated to the thickness of the deposited film. However, this thickness will be inaccurate because the crystal monitor is placed at the edge of the substrate stage, as shown in Fig. 21. A relatively large variation of film thickness, around 5 percent, can occur from the center to the edge of a 4 inch

wafer. An extreme case of this variation from center to edge can be seen in the  $\text{Ta}_2\text{O}_5$  sputtered thin film in Fig. 22. A tooling factor can be used to account for this difference in thickness. Unfortunately, the tooling factor is a function of deposition conditions such as pressure, power, temperature and target type, as well as the crystal life, making it an unreliable technique. Another problem with the crystal monitor is that the crystal can become overloaded with sputtered material over the course of a single thick deposition,



**Figure 22: Thickness variation across a sputtered  $\text{Ta}_2\text{O}_5$  thin film.**

as commonly encountered in infrared films. As the crystal becomes overloaded, the accuracy of the measurement degrades. This can be corrected by using a timed shuttering system to prevent overloading, but this type of system was not included on the crystal monitor used in the Denton Vacuum Explorer 14 magnetron sputtering system. The crystal monitor can also be affected by temperature variations during deposition, although a water cooling system was utilized in the setup.

Because of the inaccuracies of the crystal thickness monitor method, another method was developed. Instead of ending the deposition when the crystal monitor indicated the desired film thickness, the deposition was timed based on previous deposition rates measured for the sputtered material. Small pieces of substrate, called companion pieces, were marked with a series of small permanent ink marks. One or two companion pieces were then included with the substrate wafer during deposition. After the deposition was completed, a lift off process was performed with the companion pieces. The companion pieces were placed in an acetone bath and agitated in an

ultrasonic bath to dissolve the permanent ink marks. With the ink removed, the material deposited on top of the ink has nothing to adhere to and breaks free of the substrate, leaving small holes in the film where the substrate is exposed. The companion pieces were then measured with an XP-1 Ambios stylus profilometer. The profilometer uses a cantilever-type stylus, to scan across the surface of the companion piece. If scanned across one of the holes in the companion piece film, the profilometer will record the height of the step from the surface of the film down to the substrate, thus providing a measurement of the film thickness. This method was preferred over the crystal monitor because it is a direct measurement of the film thickness and does not suffer from heating or overloading problems, although a tooling factor must still be employed since the companion piece is located at the edge of the wafer. One important problem with the companion piece method is that there is no way to know during deposition whether or not the desired thickness has been reached except by timing. Run to run variations in deposition rates naturally cause errors in film thickness, which if uncorrected can profoundly affect the resulting spectrum. This lead to the development of a running filter design, as will be discussed in section 3.4.

## CHAPTER III

### Filter Designs for the Mid-Infrared (3-5 $\mu\text{m}$ ) Wavelength Region

#### 3.1 Mid-Infrared Filter Application

Filters designed for the mid-infrared region are important in night vision and thermal imaging applications. Typically, thermal imaging applications are not designed to spectrally resolve the detected wavelength. These thermal images are simply a grayscale intensity distribution. However, there are applications where it is necessary to spectrally resolve the thermal image. The simplest approach is to use a high pass and a low pass filter to split the mid-infrared band. Such filters would divide the mid-infrared band into a 3 to 4  $\mu\text{m}$  band and a 4 to 5  $\mu\text{m}$  band. These filters could be applied to the imaging sensor at the pixel level through patterning techniques, or could be used in a bulk capacity in a shuttered or rotating system.

#### 3.2 Desired High and Low Pass Filter Performance

Both high and low-pass filters were designed for the 3 to 5  $\mu\text{m}$  wavelength region, with the transition occurring at 4  $\mu\text{m}$ . The high-pass filter passes wavelengths from 4 to 5  $\mu\text{m}$  and blocks wavelengths from 3 to 4  $\mu\text{m}$ . The low-pass filter passes wavelengths from 3 to 4  $\mu\text{m}$  and blocks wavelengths from 4 to 5  $\mu\text{m}$ . (See Fig. 23) The final high-pass design was optimized using 23 layers of silicon dioxide and germanium, as shown in

Fig. 24 (a), and at total thickness of 7.34  $\mu\text{m}$ . The final low-pass design included 25 layers, as shown in Fig. 24 (b), and at total thickness of 8.14  $\mu\text{m}$ . It was desired to limit the total thickness of each filter to less than 10  $\mu\text{m}$  to allow for lift off processes required for patterning to allow the filters to be applied at the pixel level. If the total thickness were much more than 10  $\mu\text{m}$ , the lift off could become difficult. The filters were designed

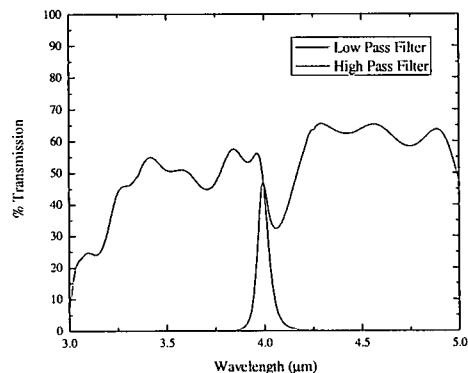
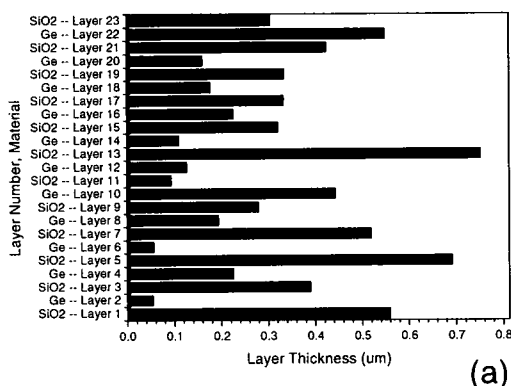
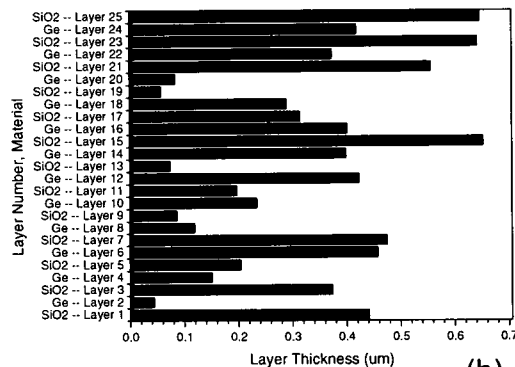


**Figure 23: Measured performance of the high- and low-pass filters.**



(a)



(b)

**Figure 24: Measured layer thickness for the high-pass (a) and low-pass (b) filters.**

and fabricated with alternating layers of silicon dioxide ( $\text{SiO}_2$ ) and germanium (Ge) sputtered thin films. Silicon dioxide and germanium were chosen because they have a large index contrast (bulk  $\text{SiO}_2$  has an index of 1.46 and bulk crystalline Ge has an index of 3.98 [3]) and are suitable for use in the mid-infrared due to their high transparency in this region. Some other materials that could have been used are silicon monoxide ( $\text{SiO}$ ,  $n=1.86$ ), silicon (Si,  $n=3.42$ ), or magnesium fluoride ( $\text{MgF}_2$ ,  $n=1.38$ ) [1],[3]. All of these materials

are transparent in the mid-infrared and are suitable for thin film deposition, by a number of methods. However,  $\text{SiO}_2$  and Ge were chosen because, as mentioned before, they have the largest index contrast, are readily available, and are easily deposited by sputtering.  $\text{SiO}_2$  was chosen over  $\text{MgF}_2$  because  $\text{SiO}_2$  is very stable and maintains its composition when sputtered, while  $\text{MgF}_2$  has a tendency to disassociate when sputtered.

### 3.3 FilmStar Design Software and Optimization Algorithms

FilmStar [10], a commercially available thin film design software package, was used in this work because it provides several optimization algorithms for practical filter designs. First, the target spectral performance must be specified using a set of data

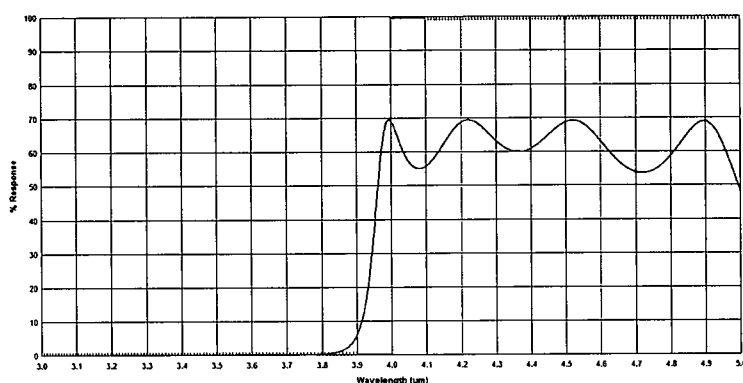


**Figure 25: High-pass filter targets and optimized design transmission plot from FilmStar. The green line is the desired target spectrum and the red line is the optimized value. [10]**

points. For the high-pass filter, the targets would be specified as in Fig. 25. FilmStar allows for up to 301 target points, with an inverse weighting system attached to each point. More importance is given

to matching targets with a low weighting value than those with a high weighting value. Generally, a weight of one is assigned to the body of the targets, while target values less than one are assigned to important features. For the high- and low-pass designs, a weighting of 0.1 to 0.5 was assigned to approximately 100 target points around the 4  $\mu\text{m}$  transition. Also, if unwanted features appeared during optimization, such as sharp

resonance peaks in the zero transmission portion of the design, the target weight in that region must be lowered to reduce the intensity of such undesired features.

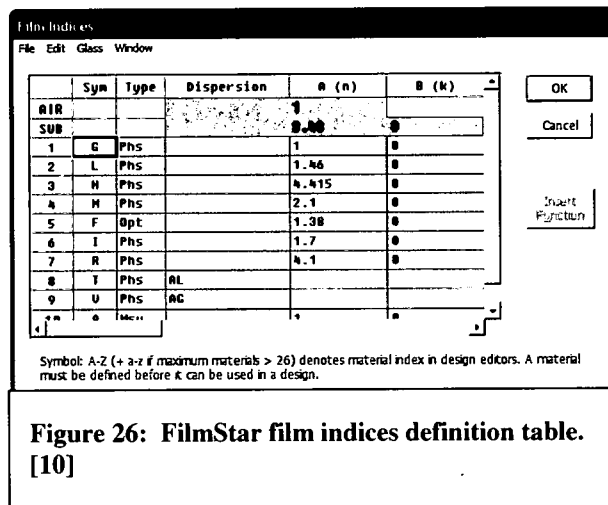


**Figure 26: FilmStar film indices definition table.**  
[10]

entered for the wavelength range of the filter, as shown in Fig. 26. Also, the properties of the substrate must be entered. The substrate type (metal or dielectric), index of refraction, thickness, and the reflection properties of the substrate, referred to as “second side compensation,” must be specified. The reflection properties of the substrate are specifically related to the back side reflection from the substrate, as shown in Fig. 27. If the back side reflection is ignored, the maximum possible transmission becomes 100

percent, but if the back side reflection is included, the maximum transmission is reduced accordingly. Ignoring the back side reflection is equivalent to assuming that a perfect antireflection coating was applied to the back side. Generally, the designs were

FilmStar also requires several other user specified parameters. The index of refraction of the materials must be specified. The index of refraction can either be specified as a single complex number (n, k) for the real and imaginary parts ignoring dispersion, or a dispersion table can be

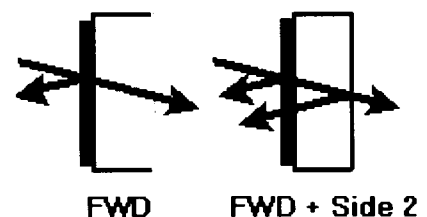


**Figure 27: Second side compensation options for FilmStar.** FWD refers to the front surface of the substrate where the filter is built. Side 2 refers to the backside of the substrate which has a reflection that can either be included or ignored in the model.  
[10]

optimized in the model by ignoring the backside reflection, and then back side reflection (typically 30% for uncoated silicon substrate) was accounted for during characterization to match the actual measured performance of the filter. It is assumed that the substrate is thick enough to not cause any appreciable interference peaks. In other words, the back side reflection is taken to be incoherent with the front side filter.

After these parameters are set, the initial design and optimization parameters can be entered into FilmStar. It was found that the starting design did not have a profound influence on the final optimized design. The optimization algorithms converged towards the same final design values for a wide range of initial designs. However, the closer the initial design is to the desired performance, the less time it will take for FilmStar to converge to an acceptable design. Generally, a 20 to 25 layer design, consisting of alternating high and low index material of 0.5  $\mu\text{m}$  thickness, is entered into FilmStar. Then any relationship between the layers is set. For instance, if it is desired for each pair of high and low index material should be held to a constant thickness, the mathematical relationship between these layers would be defined at this time. Since it was not important to produce a periodic structure, but rather a high performance structure, no such relationships were employed in our designs. The most important design features were spectral performance and ease of fabrication. Therefore, each layer was set as a variable, independent from the others. Then an optimization algorithm was selected. While FilmStar offers several optimization algorithms, the algorithms employed in this research were the simplex and genetic algorithms. Since a detailed exploration of the mathematics behind these algorithms is beyond the scope of this thesis, only an operational description is presented here.

According to Meyer, et al [11], the simplex method of optimization utilizes movement along a multi-dimensional “simplex” shape to reach the optimal value. The simplex is a three-dimensional shape defined by  $d+1$  points in a  $d$ -dimensional parameter space. An initial simplex is defined by the user, preferably one that covers the region where the optimum is located. The initial points are evaluated with a merit function. Those points that are furthest from the optimum have the largest merit function values.

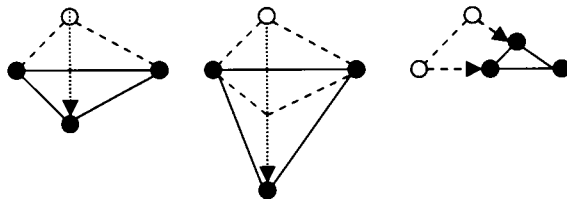


**Figure 28: Two-dimensional representation of the reflection, expansion and contraction moves in the simplex method. [11]**

All the points in the simplex, except for the point with the largest merit function, form a hyper-plane. The worst point, with the highest merit function, is reflected through the hyper-plane. This

new point, the reflection of the worst point, is evaluated. If the new point has moved in a direction that brings it closer to the optimum, then the simplex continues to expand in that direction. If not, the simplex will either do nothing or perform a contraction by drawing the reflected point closer to the hyper-plane, as shown in Fig. 28. If these actions do not bring the simplex closer to the optimum, then a  $d$ -dimensional contraction will occur. In this action, all the points in the simplex are moved towards the best point, i.e. the point with the lowest merit function. These steps continue until the merit function of the best point drops below a user defined acceptable value. The simplex could also fail if the points are contracted too close together. For the filter design process, the simplex method was terminated after the real-time update of the filter performance ceased to show significant change over several minutes.

The genetic algorithm is a global search optimization method that utilizes rules based on natural selection and genetics, as described by Wang [12]. This set of search rules is based on survival of the fittest, but that also incorporates random “mutations,” such as would occur in a biological system. An initial “population” or set of points is used to complete the necessary calculation, in this case, the “population” is made up of the individual layers of the filter, and the calculation is the transmission profile of the filter. The individual members of the population are compared, and given a statistical weighting, or “rank” as to which are the “fittest”, i.e. contribute most to the desired outcome. Two members are chosen randomly from the population to “mate” or to be combined according to a set mathematical relation to create a new data point. The points that have been assigned higher statistical fitness are more likely to be chosen. This is repeated until a new “generation” of points has been created. However, a certain percentage of anomalies are also chosen to be incorporated into each generation. These anomalies can either be members from the previous generation that pass directly into the new generation, or they can be random “mutations,” i.e. points in the new generation that are randomly altered. The new generation of points is expected to produce a more optimal result because they have been created from the “fittest” points from the previous generation. This process is repeated until acceptable convergence is achieved, or until the user defined number of generations has occurred.

The benefit of the simplex method is that it converges very quickly. However, the simplex algorithm does not allow for control of the thickness of each layer, and often produces layers that are either too thin to be measured by the available profilometer (<500 angstroms) or so thick that either film stress or even deposition time (>1  $\mu\text{m}$ )

become an issue. The genetic algorithm provides a solution to the thickness problem by allowing thickness limits to be set by the user. However, the genetic algorithm converges much more slowly, and often produces transitions that are not as sharp as those produced with the simplex algorithm.

### 3.4 User Intervention during Optimization

It was found during the filter design process that alternating between the simplex and genetic optimization algorithms, at the discretion of the user, produced better filter designs that fit more closely to the prescribed design targets. This process was developed as the need for higher performance in the fabricated filter became important.

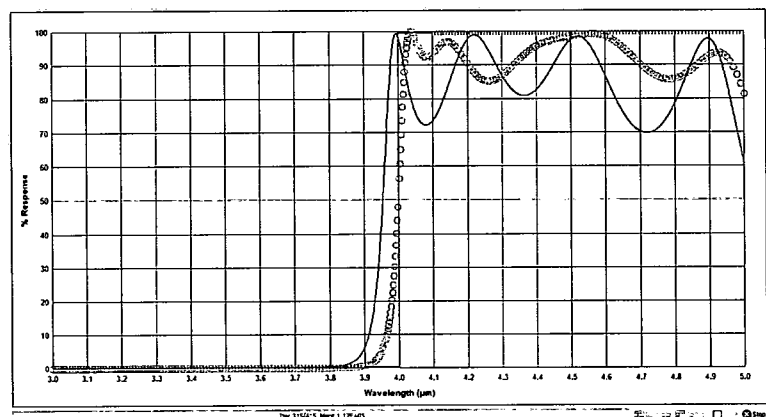


**Figure 29: FilmStar transmission plot showing the real time update of a high-pass filter during simplex optimization. [10]**

Once an optimization algorithm has been selected, the user defines the number of iterations or generations to be run, however optimization can be terminated at any time. FilmStar gives a real time output of the transmission profile of the changing design, so if the optimization algorithm slows and begins to converge before the set number of iterations, or if a problem with the design emerges, the user can terminate the process, as seen in Fig. 29. In this plot, the red line is the initial high-pass design, and the green line

is the continuously updating optimized performance. This optimized design changes with each Simplex iteration. The initial optimization process generally takes several thousand iterations, and requires alternation between the genetic and simplex algorithms and user intervention. For example, when running the simplex algorithm, as mentioned before, often layers that are too thick or too thin are produced. After a set of iterations, the user can manually alter the thicknesses of these thick or thin layers. It was found to be effective that if the user decreased the thickness of one layer, the thickness of two surrounding layers should be increased proportionally. This maintains the total design thickness and tends to cause less significant change in the design transmission performance than when simply changing the thickness of one layer at a time. Another technique used was to set layers that were near the upper or lower level of acceptable thickness as constants by removing them from the variable list before the next set of simplex iterations. If the design did not converge satisfactorily after this was done, more layers were added to the design to increase the number of variables, or occasionally reducing the number of layers caused the design to converge. If the genetic algorithm was used, the same techniques were applied, but usually all that was necessary was to change the thickness limits of all or some of the layers to achieve acceptable convergence. The thickness limits for each layer can be set independently, but generally a range of 500 angstroms to  $0.9\text{ }\mu\text{m}$  was used for all layers. If a design was not converging to high enough performance using the genetic algorithm, a few hundred iterations of the simplex algorithm were alternated with sets of genetic algorithm iterations to increase the speed of convergence and improve final performance. The design was optimized until either the transmission performance reached an acceptable

level or until further optimization was no longer possible without exceeding total or layer thickness requirements, a practical number of layers for ease of fabrication, or simply until the design began to converge at such a slow rate that it was not efficient to allow the optimization to continue. Once an acceptable design had been obtained, the filter was fabricated.

### 3.5 Real Time Design Optimization During Fabrication

Generally, multilayer dielectric filters are designed by one individual and are then passed to another individual for fabrication. Significant deviation from the target performance can occur due to the natural variations of deposition rate and refractive index that take place during fabrication. It is difficult to know these variations ahead of

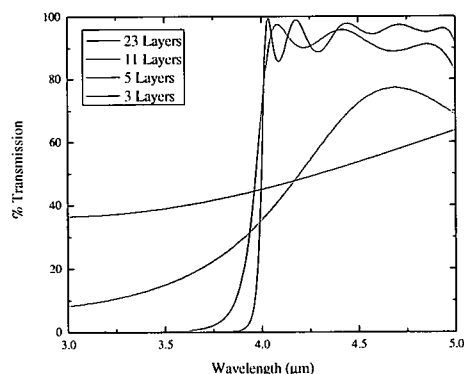


**Figure 30: Comparison of a high-pass filter model transmission profile using only 3, 5, 11, and all 23 layers.**

time, hence a real-time optimization would be highly valuable. The design could be optimized on a per-layer basis after each deposition by measuring the performance of the filter and comparing it to the model after each layer. However, this approach poses

some difficulties, especially during the first few layers, because there will be few distinctive features that could be used to match the actual performance to the model with only a few deposited layers. It is not until all the layers are considered that distinct peaks or troughs emerge that can be used to compare the actual performance to the design, as shown in Fig. 30. However, by the time

most layers are deposited, it will be difficult or impossible to repair the design in subsequent layers. Instead, the model is re-optimized after each layer deposition during fabrication, so that deviations in the measured thicknesses of deposited layers from the

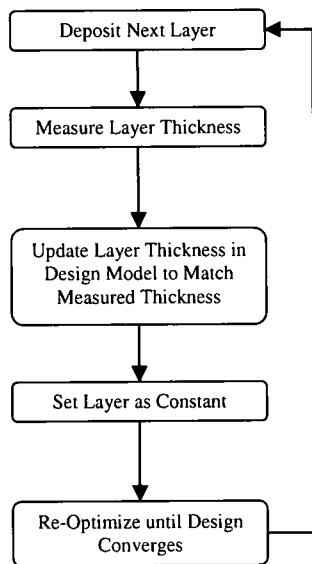


**Figure 31: Continual design re-optimization during fabrication.**

design thickness can be compensated for and overall final performance improved. The re-optimization process is described in Fig. 31.

In the past, the filter was fabricated following the pre-designed structure as closely as possible, but inevitably the deposited thicknesses of the layers would differ from the design, leading to degradation of performance. This is due to fluctuations in the deposition rate both during deposition and from one deposition to the next. The

deposition rate for germanium was found to fluctuate by as much as 17% from one deposition to the next. This can lead to a significant difference in the deposited thickness from the intended thickness of a film, because the previous deposition rate is used to calculate the deposition time for the next layer.

This can lead to the deposited thickness of each layer being off by up to 17% for germanium. The only method for managing the deposited thickness of a film was to deposit each film in partial steps. Using our real-time optimization method, each layer of the film was measured for thickness and the deposition rate was recalculated for the next layer until the desired film thickness was achieved. However, this process only works for films that have a total thickness that can be divided into layers thicker than the minimum

measurable thickness for the profilometer, 500 angstroms. This severely limits the design possibilities for the filter. In order to achieve a high performance filter design, 20 or more layers are required. This, coupled with the constraint that the total thickness of the filter be less than 10  $\mu\text{m}$ , prevents the filter layers from each being 1000 A or more in thickness.

This led to the situation where when fabricating the filter, any layer in the design that was between approximately 500 and 1000 angstroms had to be deposited in one step. If any large fluctuation of deposition rate occurred, the deposited layer could be much thicker or thinner than desired. In the case of a layer that is too thin, more material can be deposited to correct the layer. However, there is no way to salvage a layer that is too thick. If the incorrect layer was deposited early

enough in the fabrication process, it may be possible to simply restart the filter and try again, but if the mistake occurred at the end of the fabrication of the filter, the decrease in filter performance due to the incorrect layer thickness would have to be accepted. Fig. 32 shows a model of how filter performance degrades from the design model because of differences in thickness from the design to the fabricated filter. Fig. 33 shows the

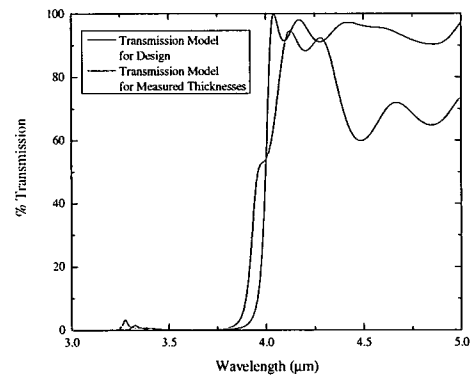


**Figure 32: Model of the degradation of filter performance when the real-time design optimization process is not implemented.**

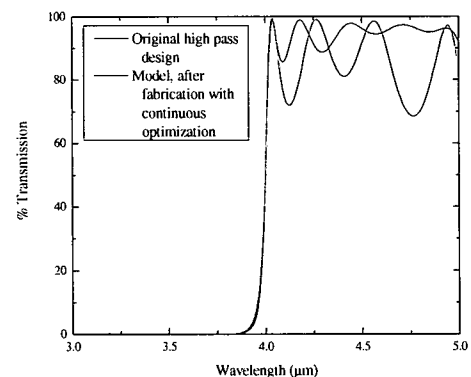


**Figure 33: Model of how filter performance is preserved by the real-time design optimization process.**

difference between the original design for filter 29 and the final performance of that filter, which had undergone continuous optimization.

## CHAPTER IV

### Analysis of Fabricated High and Low Pass Filter Performance

#### 4.1 Transmission Spectra of Selected Filters

The transmission spectra of the following filters were taken with a Fourier Transform Infrared Spectrometer (FTIR) over wavelengths of 2-7  $\mu\text{m}$ .

The first filter attempt had 6 layers of alternating  $\text{SiO}_2$  and Ge sputtered thin films. The total thickness of the filter was 2.3  $\mu\text{m}$ . The design assumed an index of refraction for  $\text{SiO}_2$  of 1.45 and for Ge of 4.0, which are commonly used values in the literature. This filter was not

designed using FilmStar.

Instead, 6 layers were chosen so that fabrication could be accomplished quickly. Then the design was created by modeling an initial design with the TMM, examining the results, and

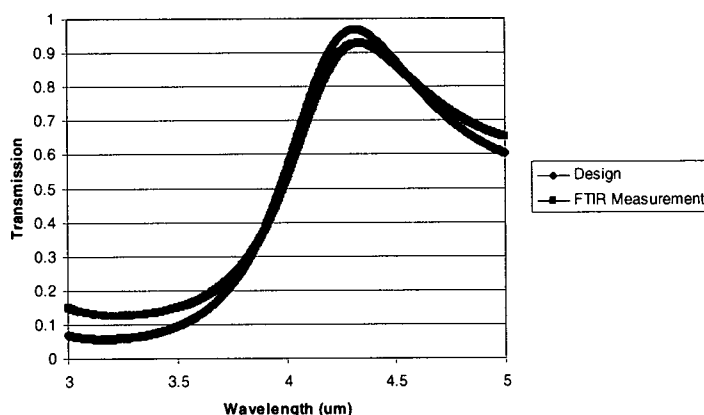


**Figure 34: The first high-pass filter attempt.**

making the best guess at how to modify the design to achieve the desired results.

As can be seen in Fig. 34, the performance of this filter is poor. The filter does not have the desired sharp transition at 4  $\mu\text{m}$  and drops to below 70 percent transmission near 5  $\mu\text{m}$ . However, the FTIR transmission data for the fabricated filter seems to match

well with the design. It is interesting to note that this filter was fabricated using the crystal monitor to end the deposition when the design layer thickness was met, and that no real-time design optimization was used on this filter. No physical measurement of the layer thicknesses was made by means of a companion piece for each layer. The close match between the design and FTIR data was encouraging, and so attempts were made to find an improved design with more layers.

After fabrication, the deposited layers of this first filter began to peel away from each other and from the substrate. This is an indication of stress in the films. The Ge films for the first filter were deposited with an Ar pressure of 2 mTorr and an RF power of 75 Watts, resulting in a deposition

rate of 1.8 angstroms/second. The SiO<sub>2</sub> films were deposited with an Ar pressure of 1.5 mTorr and an RF power of 300 Watts, resulting in a deposition rate of 0.8 angstroms/second. At the time, it was

thought that the cause of the peeling could be simply poor adhesion

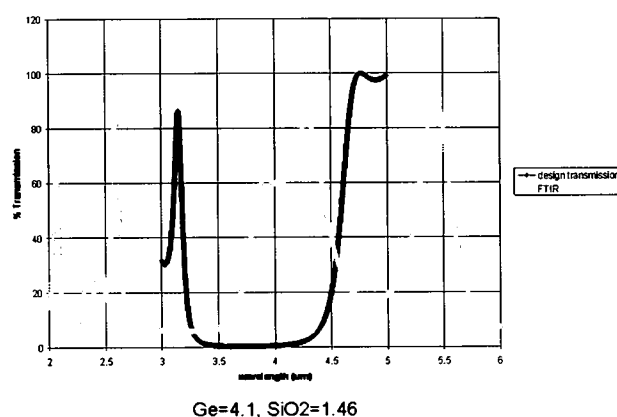


**Figure 35: Filter #2**

between Ge and SiO<sub>2</sub>, so the second filter was fabricated with thin, 300 angstrom interfacial layers of Si between each Ge-SiO<sub>2</sub> interface. The difficulty with this procedure was that the target material had to be changed after every other deposition because our currently available Denton Vacuum Explorer 14 has only two cathodes. Changing targets is not only cumbersome, but requires the chamber to be opened for long

periods of time, leading to longer pump down times and the increased risk of contamination of the deposited films. The deposition gas pressure and RF power were also changed to produce slower deposition rates in an attempt to reduce stress. When the addition of thin Si layers failed to improve adhesion, that approach was abandoned. The second filter was also fabricated using the crystal monitor to measure the layer thicknesses. The measured performance of this filter did not match the design, as seen in Fig. 35, and this led to the suspicion that the layer thicknesses measured by the crystal monitor were inaccurate. From this point on, a companion piece was used to measure the thickness of each deposited layer.

The third filter, Filter #3, was fabricated using the same design as the second filter, with the exception that the 300 angstrom thick Si layers were eliminated, to see if the slower deposition rates would lead to less stress in the deposited films. Filters #2 and #3 were deposited with 5 mTorr Ar pressure and 150 Watts RF power for SiO<sub>2</sub> and 5 mTorr Ar pressure and 40 Watts RF power for Ge. These conditions resulted in a deposition rate of approximately 0.5 angstroms/second for Ge and 0.3 angstroms/second for SiO<sub>2</sub>. Again, when the FTIR performance of the filter was measured, the transmission did not match the TMM model. This led to the suspicion that the germanium films might be oxidizing during periods when the sputtering chamber was opened to the atmosphere, leading to a change in the index of refraction. This theory was tested by changing the index of refraction of the germanium films in the TMM model and matching the results to the FTIR transmission spectra, as shown in Fig. 36. The TMM model came to a close match of the FTIR data for an index of refraction of Ge of 2.4, and an index of refraction of SiO<sub>2</sub> of 1.46. Pajasova, et. al., give the value of GeO<sub>2</sub> at 1.6 in

the infrared [13]. After this, several changes were made to avoid contamination and oxidation of the Ge films. The sputtering chamber walls, cathode shields and shutters were all cleaned and bead blasted more regularly since it was thought that any deposited  $\text{SiO}_2$  on the surfaces inside the chamber could outgas oxygen during the Ge depositions, leading to oxidation. Also, the base pressure was lowered from 9  $\mu\text{Torr}$  to 0.7  $\mu\text{Torr}$  to reduce the amount of water vapor and residual gases inside the sputtering chamber. Since the companion piece had to be removed from the chamber after each deposition,

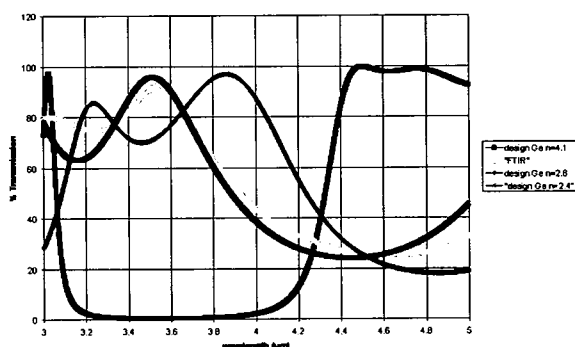


**Figure 36: Filter #3. First indication of the germanium index of refraction error.**

opening the chamber was unavoidable.

To prevent oxidation of the Ge films while the chamber was exposed to the atmosphere, a cap of 300 angstroms of  $\text{SiO}_2$  was deposited on top of each Ge film.

However, even with these changes, the measured transmission from the FTIR appeared to be the same shape as, but shifted in wavelength from, the TMM model for each filter. Also, the index of refraction of Ge required to align the model to the measured transmission spectra was different for each filter. Also, unlike Filter #3, this index of refraction was generally higher than the quoted index of refraction of 4.0 for bulk crystalline germanium. This index of refraction varied from as low as 3.72 to as high as 4.5. This increased index of refraction would indicate that the change is not due to oxidation, which would result in a lower index of refraction. While it is not uncommon for thin films deposited by different methods to have different physical and optical properties, the large variations in refractive index

observed during this study for germanium was somewhat unexpected. Although there are a few published results on sputtered germanium thin films [14],[15], there were no specific data on refractive index in the 3-5  $\mu\text{m}$  range. This was a curious observation given the fact that germanium is a widely used optical material in the infrared. However, germanium thin films are usually used for broadband applications, such as antireflection

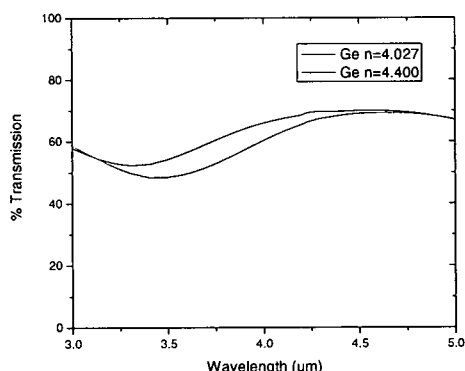


**Figure 37: For a very flat, broadband filter, small variations of the index of refraction may not be apparent.**

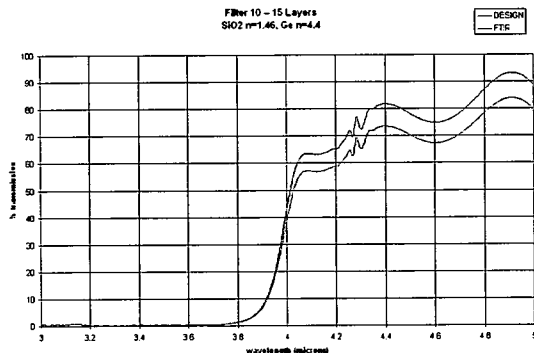
coatings, so any subtle difference in index of refraction may not have been noticed, since it manifests itself by shifting the entire transmission spectra to higher or lower wavelengths. This shift may not be apparent for very flat, broadband filters, as shown in

Fig. 37. Hence, a more thorough investigation into the question of the index of refraction of the sputtered germanium

films became justified. This topic is addressed in more detail in section 4.2.

After concluding that a powerful optimization algorithm was needed to design high and low pass filters with the very sharp transition at 4  $\mu\text{m}$ , the FilmStar software package was purchased. Using this software, several designs were created using as many as 25 layers. The FilmStar software also opened the door for the real-time design optimization concept, where the design is re-optimized to account for differences between the measured deposited thickness of a film, and the thickness prescribed by the design. This process is described in section 3.5. Before the real-time design optimization process was used, and it became apparent that significant differences in thickness

between the deposited films and the design thicknesses were occurring, each filter layer was deposited in two depositions. First, the deposition was timed for half of the total layer thickness. After this layer was measured, the second half of the deposition was timed using the latest deposition rate measured from the first half. This two step deposition process was used in the fabrication of Filter #10, which was designed to have



**Figure 38: Filter 10 FTIR measured performance compared to the model for the first 15 layers.**

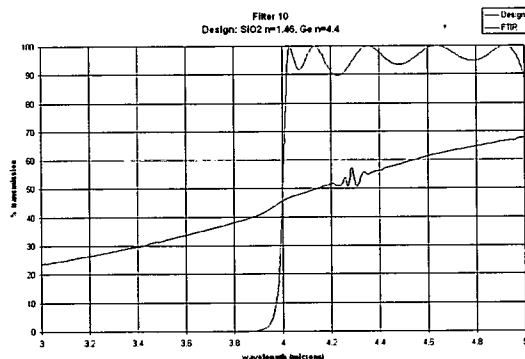


**Figure 39: Filter #10 FTIR measured performance compared to the model after the deposition of the final layer.**

24 layers. The performance of the filter was measured using FTIR half way through the deposition process, when the model indicated that there would be some identifiable spectral peaks. The measured performance of this filter matched the model for the first 15 layers with an index of refraction for germanium of 4.4, as shown in Fig. 38.

However, some problem arose during the deposition of the last nine layers because the final performance of the filter did not match the model at all, as shown in Fig. 39. One possible explanation for this failure is that one or more of the deposited layer thicknesses were different enough

from the design thicknesses that the model could not accurately describe the final performance of the filter. In fact, this is most likely the case. In layers 1 through 15, all

the deposited layer thicknesses were greater than 470 angstroms, well above the noise level of the profilometer scans. While the profilometer has the range to measure down to tens of angstroms, its accuracy is limited by the background vibration and airflow in the clean room laboratory, which leads to a high level of noise, making it difficult to measure thicknesses much less than 500 angstroms. However, on layer 18, a problem occurred. Layer 18 was a germanium layer. The first half of layer 18 was deposited, and this was measured to be 751 angstroms thick. The total desired thickness of layer 18 was 1559 angstroms, so the second deposition was set to deposit 808 angstroms of additional germanium. However, when the second companion piece was measured, the measured thickness was only 100 angstroms. This difference could be explained by the decrease in DC bias seen for the 100 angstrom deposition, versus other germanium deposition for this filter. For the other germanium depositions, the DC bias was 298-308 Volts, while for the 100 angstrom deposition, the DC bias was 267 Volts. Since DC bias is related to the deposition rate, this could explain the decreased deposition rate. This measurement is unreliable because of the noise in the profilometer measurement. But despite this, a third deposition was done in order to deposit 708 angstroms of germanium to complete the layer. This third deposition added 688 angstroms to layer 18. If all the measured thicknesses are assumed correct, the total thickness of layer 18 would have been 1539 angstroms, instead of the desired 1559 angstroms. However, because the 100 angstrom measurement from the second deposition was unreliable, there could have been significantly more or less material deposited at that time, leading to a significantly different total layer 18 thickness. Also, since this was a germanium layer, the high index of refraction material, the impact on the design is greater than if the incorrect layer were

SiO<sub>2</sub>. When mistakes are made in the high index of refraction layers, the impact on the overall performance was found to be greater.

At the time, the problem with the noise level and the 100 angstrom thickness measurement were not apparent. Instead, the failure of Filter #10 was thought to have been caused by the sum of the small deviations of each layer thickness from the design. Depositing each layer in two steps did not do much to improve the difference between the desired layer thickness and the measured deposited thickness. If the deposited film was

measured to be thinner than desired, more material could be added, but there was no solution for films that were too thick. For this reason, the real-time design optimization process was implemented. Using this process, layers that had been deposited and were too thick could be compensated for in the design.

Several more filters were designed and fabricated. Several of these filters had poor film adhesion and peeled. For this reason, the deposition conditions were varied, until finally good adhesion was achieved with conditions of

4 mTorr argon pressure, and an RF power of 180 Watts for germanium and 300 Watts for SiO<sub>2</sub>. Filters #28 and #29, low and high pass

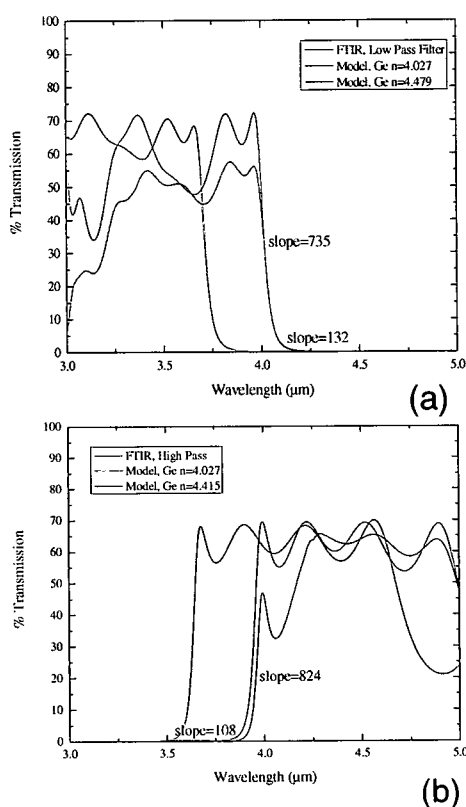


**Figure 40: Measured FTIR transmission compared to the FilmStar Model for two different values for the germanium index of refraction for low-pass filter #28 (a) and high-pass filter #29 (b).**

filters, respectively, demonstrated acceptable performance for the desired application.

The performance of Filters #28 and #29 are shown in Fig. 40 (a) and (b), respectively. Both of these filters were fabricated using the real-time design optimization concept, and were designed using an index of refraction for germanium of 4.47, and for SiO<sub>2</sub> of 1.46. This index of refraction for germanium was chosen because it provided the best match between the TMM model and the FTIR spectral data in all the previous filters fairly consistently.

The FilmStar model of the finished filters used the measured thickness of the layers obtained from the companion pieces, corrected to account for the thickness at the center of the wafer, and assumed no dispersion for either the SiO<sub>2</sub> or germanium films. As is evident from the graphs, the shape of the transmission spectra obtained by the FTIR is significantly different for Filter #29 than what is predicted by the model. This was thought to be a possible indication that the germanium films have some dispersion in the 4 to 5  $\mu\text{m}$  region, since SiO<sub>2</sub> was not expected to have any absorption in this region. The topic of dispersion in the germanium and SiO<sub>2</sub> films will be discussed in section 4.2. When the model, using the index of refraction of 4.47 for germanium, was superimposed in the FTIR transmission spectra for Filter #28, the model was slightly downshifted from the FTIR data. Changing the index of refraction of germanium to 4.479 in the FilmStar model caused the FTIR data and the FilmStar model to be aligned. There is some ambiguity in deciding when the measured and calculated spectra are aligned. The two spectra were considered to be aligned when the 4  $\mu\text{m}$  transition and the peak nearest the transition were in close alignment between the two plots. Similarly, the FilmStar model for Filter #29 was slightly upshifted for an index of refraction of 4.47 for germanium. When the index of refraction was lowered to 4.415, the FTIR transmission spectra and

the FilmStar model became aligned. In this case, since the FTIR transmission spectra was a significantly different shape from the FilmStar model, the 4  $\mu\text{m}$  transition of the FTIR data had a different slope from the model. In this case, the spectra were considered to be aligned when the peaks nearest the 4  $\mu\text{m}$  transition were aligned. From this, and other filter attempts, it was concluded that the index of refraction of sputtered germanium had an index of refraction near 4.4, but there were still cases where the index of refraction of germanium had to be lowered to near 2 to get the filter models to fit the measured FTIR data. For this reason, it became necessary to further investigate the index of refraction of germanium and  $\text{SiO}_2$ .

#### 4.2 Physical and Optical Properties of Sputtered Germanium and Silicon Dioxide Films

Based on the problems encountered with high and low pass filters described earlier, further investigation was made into the stress, composition, and index of refraction of sputtered germanium films. Investigation into the index of refraction of the sputtered  $\text{SiO}_2$  films was also made. The tensile stress in the sputtered germanium films will be discussed first, then the composition of these films will be discussed. Finally, a discussion of the dispersion of the germanium and  $\text{SiO}_2$  films will be made.

From the improved adhesion observed in filters where the germanium films were deposited at 4 mTorr and 180 Watts, it was thought that these deposition conditions resulted in low amounts of stress in the films, and this was confirmed through Raman spectroscopy. Several single layer samples of sputtered germanium films on Si substrate were fabricated under different deposition conditions. The Raman spectrum was taken for each of these films with a Renishaw inVia Reflex Micro-Raman, with a confocal

measurement depth profiling resolution of 2.5  $\mu\text{m}$ , courtesy of the University of Dayton Nanoscale Engineering Science and Technology Center (NEST lab). The Raman spectra show characteristic peaks for both the germanium thin film and the silicon substrate. For comparison, the Raman spectrum was also taken for the bulk germanium sputtering target. Fig. 41 and Table 1 show the results of the Raman spectroscopy.

**Table 1: Raman spectroscopy results for single layer sputtered germanium films. Shift in characteristic peak and full width half max of peaks.**

Deposition Conditions	Measured Film Thickness (angstroms)	Peak Location ( $\text{cm}^{-1}$ )	Shift ( $\text{cm}^{-1}$ )	Full Width at Half Max ( $\text{cm}^{-1}$ )
2mT 200W	3434	275.1	25.1	69.2
4mT 180W	3486	271.8	28.4	73.6
4mT 250W	3348	268.5	31.7	82.4
6mT 50W	3473	271.8	28.4	101.2
7mT 220W	3535	271.8	28.4	67.0
Ge Bulk Target	---	300.2	0.0	8.7

These results indicated two things. First, the shift in the position of the germanium peak for the sputtered films from that of the bulk germanium is an indication

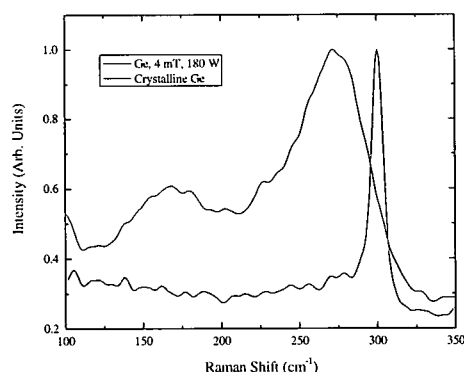


**Figure 41: Raman spectra for bulk crystalline germanium and for a germanium thin film sputtered at 4 mTorr argon pressure and 180 Watts RF power.**

of the amount of tensile stress in the sputtered films. The greater the shift, the greater the tensile stress in the film. As can be seen in Table 1, the peak shift is smallest for the film fabricated at an argon pressure of 2 mTorr and an RF power of 200 Watts, but is not much larger for 4 mTorr and 180 Watts. The results also indicate that the tensile stress increases with RF power when the argon

pressure is kept constant. Filters #4-#11, #18, #19, #20 and #22 were fabricated at 2

mTorr and 200 Watts for Ge, and 2 mTorr and 300 Watts for SiO<sub>2</sub>. High deposition rates were seen for both Ge and SiO<sub>2</sub> under these conditions (approximately 5.15 angstroms/second for germanium, and approximately 1 angstrom/second for SiO<sub>2</sub>). However, many of these filters peeled. Since no data was taken for SiO<sub>2</sub> samples to determine the stress in these films, it is possible that the stress in the SiO<sub>2</sub> films caused the poor adhesion, even though the stress in the germanium films was low. Films deposited at 4 mT, 180 Watts for germanium and 4mT, 300 Watts for SiO<sub>2</sub>, exhibited similar deposition rates (approximately 3.8 angstroms/second and 1 angstrom/second, respectively) but had improved adhesion. It is possible that the stress in the SiO<sub>2</sub> films could be reduced by increasing the argon pressure during deposition. An increase in argon pressure results in more scattering of the sputtered atoms before they hit the substrate, and could possibly result in fewer voids in the film, leading to lower stress. Second, these results indicate that the sputtered germanium films may be amorphous. The Raman peaks for all of the sputtered germanium films were significantly broadened compared with the crystalline germanium target peak. This broadening is an indication that the sputtered germanium films are amorphous or polycrystalline in nature, and are certainly not single crystalline. This is to be expected, because the sputtering process should not result in crystalline films. This is also supported by the work of Drevillon, et. al. [14].

However, the possibility of contaminated germanium films should not be disregarded. Contamination sources could come from oxygen or nitrogen from the background gases or the sputtering gas (Ar), or structural components of the sputtering cathode such as stainless steel and copper. The same single film germanium sample,

fabricated at 4 mTorr and 180 Watts, was then tested for contamination with energy dispersive X-ray spectroscopy using a Genesis 2000 EDAX EDS integrated with an EVO-XVP Zeiss ESEM, capable of detecting all elements with an atomic number greater than or equal to 5, courtesy of the NEST lab and Scott Streiker. As discussed in chapter 2, contamination can lead to significant changes in the index of refraction of a film. This test was used to rule out contamination as the cause of the increase in the index of refraction of the sputtered films from that of bulk crystalline germanium. The results of this test are shown in Fig. 42. This test determined that only germanium and silicon were present in the sample, which indicates that there is no significant contamination in the

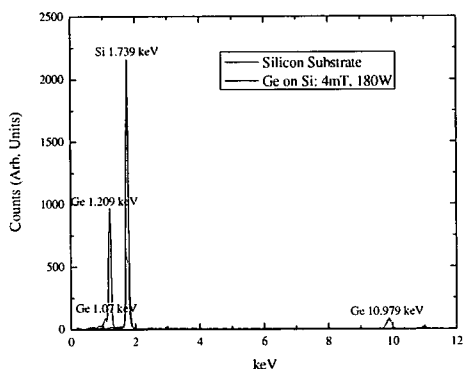


**Figure 42: Energy dispersive X-ray (EDS) spectra of a single sputtered germanium thin film on a silicon substrate.**

germanium films that could cause a noticeable change in the index of refraction.

As is apparent from the results in section 4.1, variations in the index of refraction of the sputtered Ge and SiO<sub>2</sub> films are a possible explanation for the apparent shift between the FilmStar transmission model and the measured transmission spectra of the finished devices. Assuming that the

sputtered germanium films are indeed amorphous or possibly polycrystalline, as was indicated by the Raman spectroscopy data presented previously, the index of refraction of the sputtered germanium could in fact be higher than that of bulk crystalline germanium. Silicon exhibits similar behavior. Amorphous silicon has an index of refraction of 3.84 at a wavelength of 4  $\mu\text{m}$  while crystalline silicon has an index of refraction of 3.43 at 4  $\mu\text{m}$

[16]. The index of refraction and optical dispersion of crystalline germanium and silicon is very well established [17]. The index of refraction of crystalline germanium ranges from 4.04 to 4.017 in the 3 to 5  $\mu\text{m}$  region. However, there is only a handful of published information about amorphous or sputtered thin film germanium. Amorphous silicon, on the other hand, has been exhaustively studied owing to its wide applications in solar cells and displays [18]. Since amorphous silicon exhibits a higher refractive index than crystalline silicon, it would be reasonable to draw similar conclusions for germanium owing to the similarities in crystal structure and chemical properties between the two materials. In [14], germanium was sputtered keeping the substrate temperature within 160 to 280°C and no substrate bias, and spectroscopic investigation revealed that the morphology of the films is fairly amorphous. In [14] they also demonstrated the threshold energy for crystallization decreases with the substrate temperature. However, this paper did not investigate the refractive index of the germanium films in the 3-5  $\mu\text{m}$  region. Amorphous germanium may also display different optical properties from crystalline germanium. An example of this is that the density of amorphous germanium can be as much as 9% greater than crystalline Ge [19].

Because of the strong evidence that the sputtered germanium films had a larger index of refraction than what was quoted for bulk crystalline germanium, errors in thickness measurement were not considered to be the cause of the shift between the measured and modeled transmission spectra of our filters. Another reason that possible errors in the thickness measurement were not considered was because the shape of the measured transmission profile was generally very close to the FilmStar model, with the entire profile shifted in wavelength. When variations in thickness were simulated in

FilmStar, the shape of the transmission profile changed significantly. In the model, thickness variations were not seen to simply shift the transmission spectra in wavelength without changing the shape of the profile. For this reason, thickness measurement error was not considered to be an important factor.

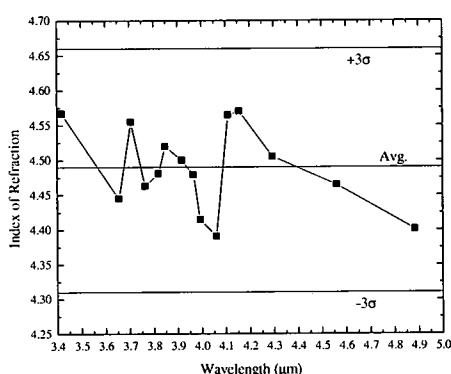


**Figure 43: Estimated dispersion in the real part of the index of refraction of sputtered germanium.**

However, when the thicknesses were left unchanged, but the index of refraction was varied in the model, it was observed that the shape of the transmission profile was preserved, but the entire profile shifted to higher wavelengths with higher Ge index, and to lower wavelengths with lower Ge index. The Ge index of refraction was chosen for investigation

because the index of refraction of the sputtered SiO<sub>2</sub> films had been reliably determined and was found to be repeatable. An initial estimate of the index of refraction of the germanium films was achieved by changing the index of refraction of germanium in the FilmStar model of the filter to cause the model to align with the FTIR transmission spectral performance of the fabricated filter. An estimate of the dispersion of the sputtered germanium was obtained by aligning several peaks in the FTIR and model spectra by means of changing the index of refraction in the model for Filters #28 and #29. The index of refraction needed to shift the model to align with a peak at a particular wavelength in the FTIR spectra was taken to be an estimate of the index of refraction at the wavelength of the peak. The estimated dispersion for the real part of the index of refraction of the sputtered germanium is shown in Fig. 43. The results of this estimation

process determined that the real part of the index of refraction of sputtered germanium lies between 4.31 and 4.66, with an average of 4.49. These results seemed to agree with several of the filters that had been successfully fabricated.

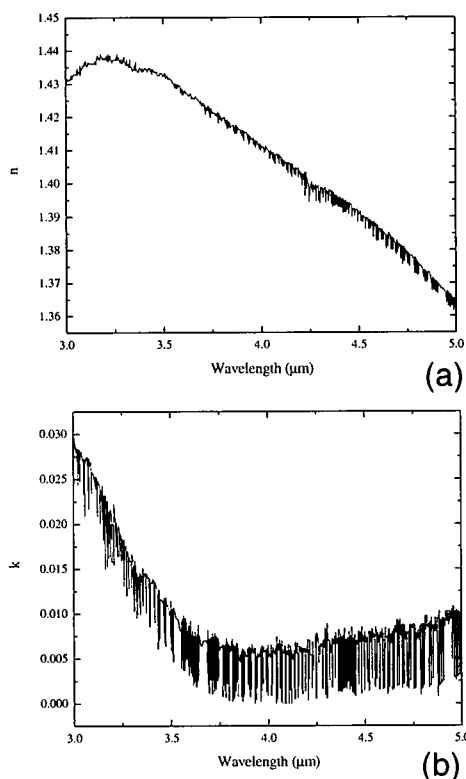


**Figure 44: Real (a) and imaginary (b) parts of the index of refraction of sputtered SiO<sub>2</sub> in the 3-5 μm region from ellipsometry data.**

and SiO<sub>2</sub> are given in Figs. 44 and 45. From this data, it is evident that the assumed index of refraction of SiO<sub>2</sub> also exhibits some variations. The sputtered SiO<sub>2</sub> has a small nonzero imaginary index in the 3-5 μm region, as does sputtered germanium. The real part of the index of refraction for sputtered SiO<sub>2</sub> ranges from 1.43 at 3 μm to 1.36 at 5 μm, and the real part of the index of refraction for sputtered germanium ranges from 4.35 at 3 μm to 4.28 at 5 μm in the 3 to 5 μm wavelength region. These indices of refraction

To test this method of index of refraction approximation, our samples were sent to the University of Nebraska-Lincoln Department of Electrical Engineering Nebraska Center for Materials and Nanoscience for ellipsometry measurement in the 3 to 5 μm region. These measurements were performed by Dr. Mathias Schubert and T. Hoffman of the University of Nebraska-Lincoln. The samples were single layers of sputtered germanium films on silicon substrates, and single layers of sputtered SiO<sub>2</sub> films on silicon substrates. The dispersion results of the ellipsometry for both germanium

are lower than what had been used in the FilmStar filter models (1.46 for SiO<sub>2</sub> and 4.47 for Ge).

These dispersion files were then used into the FilmStar model of Filter #29 to see if this would cause the model to better match the FTIR data, since the FTIR performance of Filter #29 was so different from the original model using an index of 4.47. As shown in Fig. 46 (a), this was not the case. The model did not match the FTIR for Filter #29 with the addition of the dispersion for Ge and SiO<sub>2</sub>. The same was also true for Filter

#28, as shown in Fig. 46 (b). For this reason, no conclusions can be drawn from the ellipsometry results at this time. It is possible that if some data smoothing is performed on the ellipsometry results a better match may be achieved. However, this discrepancy between the model, using dispersion, and the measured performance of Filters #28 and #29 could also indicate an issue with the measurement of the thickness of the deposited films. As indicated previously, the sputtered germanium film thickness over a 3 inch wafer varies by approximately 5 percent from the center to the edge of the wafer. This variation is

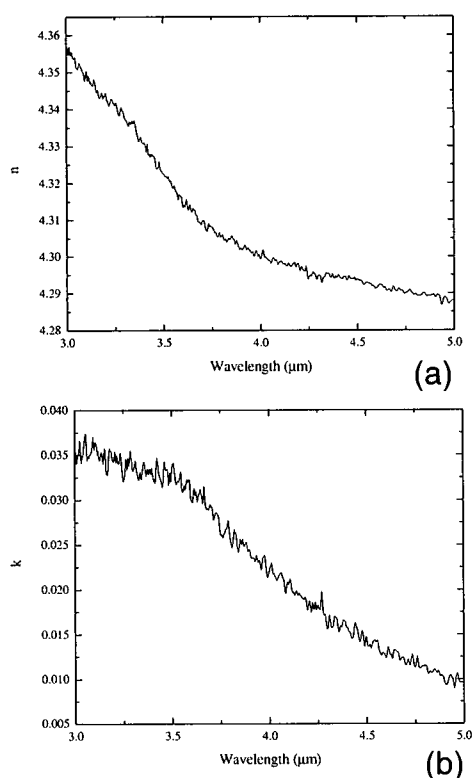


**Figure 45: Real (a) and imaginary (b) parts of the index of refraction of sputtered germanium in the 3-5 μm region from ellipsometry data.**

approximately 3 percent for SiO<sub>2</sub>. However, it is possible that this tooling factor varies from run to run. It may be the case that when dispersion data is entered into the model,

the contributions from these small errors in thickness measurement are amplified by the FilmStar model. Errors in the tooling factor could be identified as the cause of the mismatch by studying the variation of the tooling factor over several deposition runs. The layer thicknesses in a FilmStar model could then be varied by these tooling factors to see if significant changes in the shape of the model transmission profile occur, similar to those observed in Filters #28 and #29.

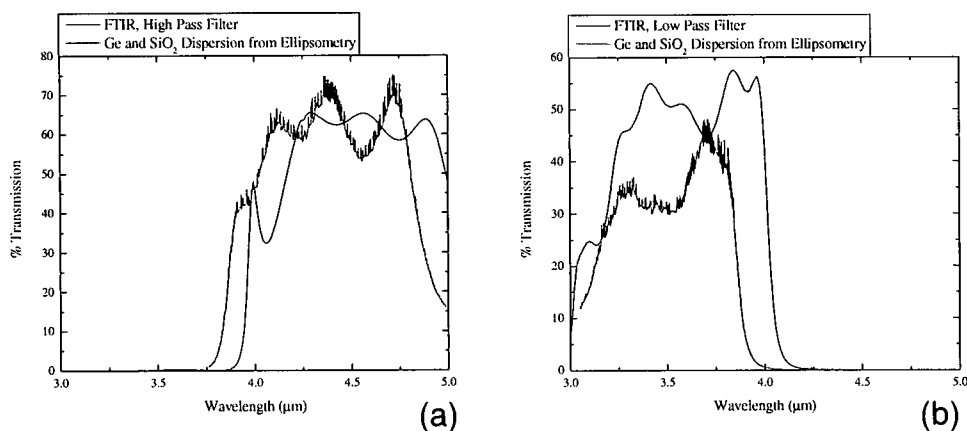


**Figure 46: Filter #29 (a) and Filter #28 (b) FTIR transmission spectra compared to the FilmStar model using dispersion for Ge and SiO<sub>2</sub>.**

## CHAPTER V

### Conclusions

In this thesis, it has been shown that the real-time design optimization process can effectively preserve the performance of the original design of an optical interference filter during the fabrication process. The real-time design optimization process can account for variations in the deposition rate, leading to deposited layers that are much thicker or thinner than prescribed by the original filter design, by allowing the design to be optimized after each deposition. This method can be implemented as long as appropriate design optimization software and an accurate means of measuring the deposited thicknesses are available. The flexibility provided by the real-time design optimization method leads not only to better performance, especially of sharp edge filters, but also saves time and prevents waste. Prior to the implementation of this method, when a deposited layer was much thicker than required by the design, the entire filter would have to be abandoned and the process restarted. Since a single filter growth could take as much as five days, if the error occurred far enough into the fabrication process, this could result in several wasted days of work in addition to wasted materials and laboratory resources.

The real-time design optimization process was later successfully used to design and build another high-performance low-pass short-wave infrared filter for the 1 to 5  $\mu\text{m}$

wavelength region. The filter consisted of 15 layers of alternating Si and SiO<sub>2</sub>, and was designed to have a sharp transition at 2.5  $\mu\text{m}$ . Since the dispersion of the index of refraction of both Si and SiO<sub>2</sub> are well known, there was no issue of the measured performance of the filter being shifted in wavelength from the design model or the problems encountered with germanium. The dispersion for both Si and SiO<sub>2</sub> were used in the FilmStar model, rather than just the real part of the index of refraction. The result of applying the real-time design optimization to the fabrication of this filter is shown in Fig. 47. There is good correspondence between the measured filter performance (denoted

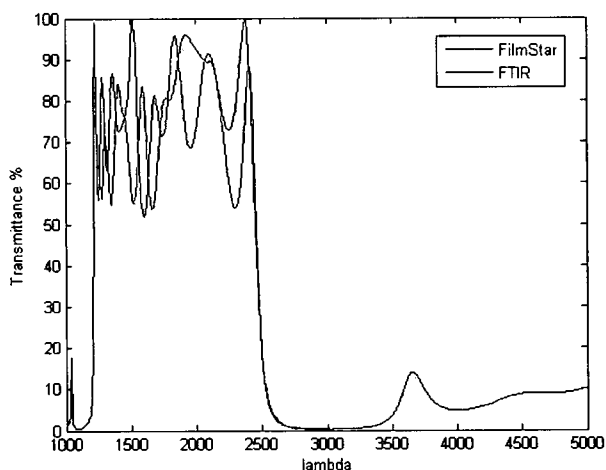


**Figure 47: High performance low-pass filter fabricated using the real-time design optimization process. Wavelength in nm.**

by FTIR) and the FilmStar model (using the measured thicknesses of the deposited layers). While the percent transmission of the pass band has decreased to approximately 50 percent at a few points, the sharp transition at 2.5  $\mu\text{m}$  has been preserved. Since it is the transition, and not the total transmission, that was required for

this filter, the real-time design optimization process can be considered successful in this case, also.

The main reason that the measured performance of the filters presented in this thesis did not match the model (TMM or FilmStar) was that there continues to be some ambiguity as to the index of refraction of sputtered germanium. The estimate of the

dispersion for germanium was gained by aligning the transmission profile of the model to the measured transmission of the filter by means of varying the index of refraction of germanium in the model. This estimate placed the index of refraction of sputtered germanium, in the 3 to 5  $\mu\text{m}$  region, between 4.31 and 4.66, with an average of 4.49. The results of a detailed ellipsometry study provided a dispersion curve for the sputtered germanium, in the same wavelength region, which ranged from 4.35 at the low wavelength end, and 4.28 at the high wavelength end. The lower limit of the estimated index of refraction falls within the range of indices of the dispersion curve. Also, contamination was considered as a possible cause, but was later ruled out as a cause of the higher index of refraction of germanium by the results of the energy dispersive X-ray spectroscopy. From this, it can be concluded that the index of refraction of sputtered germanium is greater than that of bulk crystalline germanium, with its precise value somewhat unknown at this time, and highly dependent on the deposition conditions.

Such a large difference in the index of refraction has a significant impact on the filter design process. When a filter is designed using a smaller index of refraction (such as for crystalline Ge), when it is fabricated, the measured transmission profile will be upshifted in wavelength from the design model. If this occurs for a sharp edge filter with a transition at a specific wavelength, the transition will be shifted to a higher wavelength, resulting in the failure of the device to meet the required performance for the given application. However, some ambiguity remains as to the correct index of refraction of sputtered germanium. Since the dispersion provided by the ellipsometry test failed to align the FilmStar model to the measured transmission profile of either Filter #28 or #29,

no clear conclusions could be drawn from the ellipsometry data for either germanium or  $\text{SiO}_2$ .

It was determined, based on the number of sputter conditions tested, that an argon pressure of 4 mTorr and a RF power of 180 Watts for germanium gives the best film adhesion for the filters fabricated in this research. From the Raman spectroscopy study, it can be concluded that sputtered germanium films are under tensile stress, which can lead to poor film adhesion. It can also be concluded from the broadening of the Raman peak for sputtered germanium that sputtered germanium is not crystalline, but is either amorphous or polycrystalline.

Since it has been concluded that sputtered germanium has a higher index of refraction than its bulk crystalline form, it is possible that like sputtered silicon, sputtered germanium has an amorphous structure. Future research should focus on determining the crystal structure of the sputtered germanium films, as a function of the sputtering conditions. It is possible that some sputtering conditions lead to highly amorphous germanium films, while other lead to polycrystalline films. Another ellipsometry study could be done, also as a function of the sputtering conditions, to determine if the dispersion varies for films sputtered under different conditions. Due to the necessity for accurate index of refraction data in filter design, and due to the importance of germanium for mid-infrared filtering applications, it is important to continue this investigation for a more thorough understanding of the optical properties of germanium thin films.

## BIBLIOGRAPHY

- [1] Smith, Warren J. Modern Optical Engineering, Third Edition. New York: McGraw-Hill, 2000. pp. 200-211.
- [2] A. Sarangan, "Transfer Matrix Method," Integrated Optics EOP-604, 8 Nov. 2005, pp. 55-57.
- [3] Campbell, Stephen A. The Science and Engineering of Microelectronic Fabrication, Second Edition. New York: Oxford University Press, 2001.
- [4] Andrew M. Sarangan, "Nano-Fabrication." [class notes], EOP 695-02, spring semester, 2007.
- [5] "Turbomolecular Pump." *Wikipedia*. 2 March 2007. 4 April 2007. <[http://en.wikipedia.org/wiki/Turbomolecular\\_pump](http://en.wikipedia.org/wiki/Turbomolecular_pump)>
- [6] G. Levi, "Combination of turbomolecular pumping stages and molecular drag stages," J. Vac. Sci. and Technol. A, Vol. 10, No. 4, 16 Dec. 1991, pp. 2619-2622.
- [7] P. Duval, A. Raynaud and C. Saulgeot, "The molecular drag pump: Principle, characteristics, and applications," J. Vac. Sci. and Technol. A, Vol. 6, No. 3, 9 Nov. 1987, pp. 1187-1191.
- [8] "Molecular Drag Pumps- MDP series - Adixen by Alcatel Vacuum Technology." *West Technology Systems Limited*. 4 April 2007. <<http://www.west-technology.co.uk/alcatel/molecuredrag.htm>>
- [9] Sarangan, Andrew M. "Denton Explorer 14 Acceptance." 2005. 4 April 2005. <<http://homepages.udayton.edu/~sarangam/nanofab/>>
- [10] FTG Software Associates. (2006) FilmStar [computer software]. Princeton, NJ: FTG Software Associates. (Version 2.40.0404)
- [11] H. Meyer, O. Biermann, R. Faller, D. Reith and F. Muller-Plathe, "Coarse graining of nonbonded inter-particle potentials using automatic simplex optimization to fit structural properties," J. Chem. Phys., Vol. 113, No. 15, 15 Oct. 2000, pp. 6264-6275.

[12] Q. J. Wang, "Using genetic algorithms to optimize model parameters," *Environmental Modelling and Software*, Vol. 12, No. 1, 1997, pp. 27-34.

[13] L. Pajasova, D. Chvostova, L. Jastrabik and J. Polach, "Optical properties of reactively sputtered GeO<sub>2</sub> in the vacuum ultraviolet region," *Journal of Non-Crystalline Solids*, Vol. 182, 22 Sept. 1994, pp. 286-292.

[14] B. Drevillon and C. Godet, "In situ investigation of the microcrystalline germanium nucleation and growth process," *J. Appl. Phys.*, Vol. 64, No. 1, 1 Jul. 1988, pp. 145-151.

[15] R. W. Collins, H. Windischmann, J. M. Cavese and J. Gonzalez-Hernandez, "Optical properties of dense thin-film Si and Ge prepared by ion-beam sputtering," *J. Appl. Phys.*, Vol. 58, No. 2, 15 July 1985, pp. 954-957.

[16] Windt, David. Ed. "Optical constants for amorphous evaporated Si." *Luxpop*. 4 April 2007. <[http://www.luxpop.com/Materials/a-Si\\_palik.nk](http://www.luxpop.com/Materials/a-Si_palik.nk)>

Data table compiled by Luxpop from:

Palik, Edward D. *Handbook of Optical Constants of Solids*. Orlando: Academic Press, 1985.

[17] S. Adachi, "Model dielectric constants of Si and Ge," *Phys. Rev. B*, Vol. 38, No. 18, 15 Dec. 1988, pp. 12966-12976.

[18] D. R. McKenzie, N. Savvides, R. C. McPhedran, L. C. Botten and R. P. Netterfield, "Optical properties of a-Si and a-Si:H prepared by DC magnetron techniques," *J. Phys. C: Solid State Phys.*, Vol. 16, 29 March 1983, pp. 4933-4944.

[19] J. R. Blanco, P. J. McMarr, J. E. Jehoda, K. Vedam and R. Messier, "Density of amorphous germanium films by spectroscopic ellipsometry," *J. Vac. Sci. Technol. A* 4(3), May/Jun 1986, pp. 577-582

R0025 9313S